

INVESTIGATION OF THE ELECTRICAL PROPERTIES OF $(\text{IN}_x\text{GA}_{1-x})_2\text{O}_3$ ALLOYS
GROWN USING PULSED LASER DEPOSITION

by

Puja Rani Saha, B.S.

A thesis submitted to the Graduate Council of
Texas State University in partial fulfillment
of the requirements for the degree of
Master of Science
with a Major in Engineering
December 2022

Committee Members:

Ravi Droopad, Chair

Ariful Haque, Co-Chair

William A Stapleton

COPYRIGHT

by

Puja Rani Saha

2022

FAIR USE AND AUTHOR'S PERMISSION STATEMENT

Fair Use

This work is protected by the Copyright Laws of the United States (Public Law 94-553, section 107). Consistent with fair use as defined in the Copyright Laws, brief quotations from this material are allowed with proper acknowledgement. Use of this material for financial gain without the author's express written permission is not allowed.

Duplication Permission

As the copyright holder of this work I, Puja Rani Saha, refuse permission to copy in excess of the "Fair Use" exemption without my written permission.

ACKNOWLEDGEMENTS

At first, I would like to express my sincere gratitude towards Dr. Ravi Droopad for being my research advisor and for giving me the opportunity to work with his research team. His continuous support and expertise have been extremely helpful, and without his kind encouragement, I would not have completed this two years degree smoothly.

I would also like to thank my co-supervisor Dr. Ariful Haque for supporting me throughout the completion of my thesis and my committee member Dr. William A Stapleton for his thoughtful comments and insightful ideas. Special thanks to the entire SRO team, especially Dr. Casey Smith, for their continuous technical assistance with all equipment and technological issues. Secondly, I would like to thank my colleagues Dr. Dalim Mia, Brian Samuels, Sourav Das, Abdul Ahad Talukder, Pallab Kumar Sarkar, Imteaz Ahmed, and Saif al Taqy for always helping me in all matters in our lab.

I would like to thank my parents for bringing me into the world and giving me opportunity to pursue my dreams. Last, but not least, special thanks to my husband and colleague Jibesh Kanti Saha for his continuous support in my research work through good and bad times.

Finally, I want to thank the Department of Defense for funding our project under grant number W911NF-20-1-0298.

TABLE OF CONTENTS

	Page
ACKNOWLEDGEMENT	iv
LIST OF TABLES	vii
LIST OF FIGURES	viii
ABSTRACT	xi
CHAPTER	
1. INTRODUCTION	1
2. LITERATURE REVIEW	5
2.1 Crystal Structure of β -Ga ₂ O ₃	5
2.2 Material Properties of β -Ga ₂ O ₃	7
2.3 Crystal Structure of In ₂ O ₃	13
2.4 Material Properties of In ₂ O ₃	15
2.5 Alloy of (In _x Ga _{1-x}) ₂ O ₃	15
3. GROWTH AND CHARACTERIZATION TECHNIQUES.....	19
3.1 Deposition Technique	19
3.1.1 Pulsed Laser Deposition (PLD)	19
3.1.2 Target Preparation.....	22
3.2 Characterization	22
3.2.1 X-ray Diffraction (XRD)	22
3.2.2 Ellipsometry	24
3.2.3 Physical Property Measurement System (PPMS).....	26
3.2.4 X-ray Photoelectron Spectroscopy (XPS)	28
4. RESULT AND DISCUSSION	31
4.1 Experimental	31
4.2 Impact of Growth Parameters	32
4.3 Effect of Homoepitaxial buffer layer on defect reduction in (In _x Ga _{1-x}) ₂ O ₃ alloy.....	50

5. CONCLUSION AND FUTURE WORK	54
REFERENCES	56

LIST OF TABLES

Table	Page
2.1. Lattice parameters for all Ga ₂ O ₃ polymorphs.....	5
2.2. Comparison of β -Ga ₂ O ₃ with other leading semiconductor materials.....	11
2.3. Lattice and positional parameters for different phases of In ₂ O ₃	13
4.1. Materials properties of (In _x Ga _{1-x}) ₂ O ₃ at a fixed pressure of 5x10 ⁻² torr and variable substrate temperatures.....	37
4.2. Materials properties of (In _x Ga _{1-x}) ₂ O ₃ at two fixed temperatures of 600°C and 500°C with variable oxygen inflow	37

LIST OF FIGURES

Figure	Page
1.1. Applications of WBG for power electronics	3
2.1. (a) Crystal structure of β -Ga ₂ O ₃ showing O and Ga sites. (b) Ga (1) is the tetrahedral and Ga (2) is the octahedral site are the two-fold Ga sites, and (c) O (1) and O (3) are the two tri-coordination sites and O (2) is the four-coordination site.....	6
2.2. Thermal conductivity of β -Ga ₂ O ₃ single crystal at different temperatures	8
2.3. Theoretical ideal performance limits of β -Ga ₂ O ₃ power devices against other major semiconductors	10
2.4. Crystal structure of cubic bixbyite In ₂ O ₃ with the b and d sites	14
3.1. Schematic diagram of PLD system.....	20
3.2. Schematic diagram demonstrating Bragg's law	23
3.3. Configuration of ellipsometry.....	25
3.4. Illustration of the sample geometry for Van der Pauw (a) resistivity (b) Hall measurement	27
3.5. Processes that result from X-ray bombardment of a surface include (a) emission of a photoelectron, (b) x-ray fluorescence, and (c) emission of an Auger electron.....	30
4.1. (a) XRD measurement of (In _{0.25} Ga _{0.75}) ₂ O ₃ grown at different substrate temperatures and (b) corresponding FWHM measurement of monoclinic and cubic plane	33
4.2. (a) XRD measurement of (In _{0.25} Ga _{0.75}) ₂ O ₃ grown at different oxygen inflow with fixed substrate temperature of 600°C and (b) corresponding FWHM measurement of monoclinic (β) and cubic (c) plane	34
4.3. (a) XRD measurement of (In _{0.25} Ga _{0.75}) ₂ O ₃ grown at different oxygen inflow with fixed substrate temperature of 500°C and (b) corresponding FWHM measurement of monoclinic (β) and cubic (c) plane	35

4.4. Temperature Vs Resistivity measurement of the samples grown at various oxygen pressure and at fixed substrate temperature of (a) 600°C and (b) 500°C	39
4.5. Temperature Vs Mobility measurement of the samples grown at various oxygen pressure and at fixed substrate temperature of (a) 600°C and (b) 500°C	41
4.6. Temperature Vs Carrier Concentration and Mobility measurement of the samples grown at various oxygen pressures and at fixed substrate temperatures of (a) 600°C and (b) 500°C.....	42
4.7. High resolution O1s core level XPS spectra of (InGa) ₂ O ₃ for various oxygen partial pressure (a) 1x10 ⁻² torr (b) 2x10 ⁻² torr (c) 3x10 ⁻² torr and (d) 5x10 ⁻² torr respectively with a fixed substrate temperature of 600°C	43
4.8. High resolution O1s core level XPS spectra of (InGa) ₂ O ₃ for various oxygen partial pressure (a) 1x10 ⁻² torr (b) 2x10 ⁻² torr (c) 3x10 ⁻² torr and (d) 5x10 ⁻² torr respectively with a fixed substrate temperature of 500°C	45
4.9. High resolution O 1s core level XPS spectra of (InGa) ₂ O ₃ for various oxygen partial pressure (a) 3x10 ⁻² torr (b) 5x10 ⁻² torr with fixed substrate temperature of 600°C. (c) 3x10 ⁻² torr and (d) 5x10 ⁻² torr with a fixed substrate temperature of 500°C....	46
4.10. High resolution In 3d core level XPS spectra of (InGa) ₂ O ₃ for various oxygen partial pressure (a) 1x10 ⁻² torr (b) 2x10 ⁻² torr (c) 3x10 ⁻² torr and (d) 5x10 ⁻² torr respectively with a fixed substrate temperature of 600°C	48
4.11. High resolution Ga3d _{5/2} XPS spectra of (InGa) ₂ O ₃ for various oxygen partial pressure (a) 1x10 ⁻² torr (b) 2x10 ⁻² torr (c) 3x10 ⁻² torr and (d) 5x10 ⁻² torr respectively with a fixed substrate temperature of 600°C	49
4.12. XRD measurement of (InGa) ₂ O ₃ thin films with and without buffer layer grown at (a) substrate temperature of 600°C and oxygen partial pressure of 5x10 ⁻² torr (b) substrate temperature of 500°C and oxygen partial pressure of 3x10 ⁻² torr	50
4.13. Temperature vs resistivity measurement of (InGa) ₂ O ₃ thin films with and without buffer layer grown at (a) substrate temperature=600°C and oxygen partial pressure= 5x10 ⁻² torr (b) substrate temperature=500°C and oxygen partial pressure=3x10 ⁻² torr	51

4.14. Temperature vs mobility measurement of (InGa) ₂ O ₃ thin films with and without buffer layer grown at (a) substrate temperature=600°C and oxygen partial pressure= 5x10 ⁻² torr (b) substrate temperature=500°C and oxygen partial pressure=3x10 ⁻² torr	52
4.15. High resolution O1s core level XPS spectra of (InGa) ₂ O ₃ grown at fixed substrate temperature of 600°C and oxygen partial pressure of 5x10 ⁻² torr (a) without buffer layer (b) with buffer layer	53
4.16. High resolution O1s core level XPS spectra of (InGa) ₂ O ₃ grown at fixed substrate temperature of 500°C and oxygen partial pressure of 3x10 ⁻² torr (a) without buffer layer (b) with buffer layer	53

ABSTRACT

Wide bandgap semiconductor materials are gaining popularity because of their favorable features for increased power and high breakdown performance. Beta-gallium oxide (β -Ga₂O₃) is one such material with direct bandgap of 4.9eV having exceptional thermal and chemical stability. Materials that can preserve favorable energy alignment when manufacturing heterojunctions and alloys are needed to improve device performance. Thus, studying the bandgap engineering susceptibility and surface electrical characteristics of In₂O₃ and β -Ga₂O₃ alloys can lead to the discovery of a plethora of new potential applications. (In_xGa_{1-x})₂O₃ alloys have highly tunable electrical and optical properties that can be used in transparent conductor technologies and solar-blind photodetectors. As a result, it is critical to develop an understanding of the structural and electrical behavior of these metal oxide alloys. In this research, alloys of Ga₂O₃ with In₂O₃, ternary (In_xGa_{1-x})₂O₃ were grown for x =25% as a function of growth parameters such as substrate temperature (T_s), and oxygen partial pressure (P_{o2}) using Pulsed Laser Deposition (PLD) technique. Amorphous to crystalline phase transformation was observed with increasing substrate temperature. Crystalline phases were detected representing both the monoclinic and cubic bixbyite phases. Ellipsometry study showed a slight thickness variation due to evaporation of volatile Ga₂O and In₂O suboxides. Temperature dependent Hall measurement analysis showed mobility and resistivity of the alloys are of the order ~ 14-30 cm²/Vs and ~7×10⁻²-9×10⁻² Ω.cm respectively. Higher mobility was observed for the amorphous alloys compared to the crystalline samples. X-

ray photoelectron spectroscopy (XPS) analyses indicated that the $(\text{In}_x\text{Ga}_{1-x})_2\text{O}_3$ alloy contains a mixture of Ga and In cation valence states and oxygen vacancies were reduced when the oxygen partial pressure during deposition was increased. The reduction of the oxygen vacancies was attributed to the suppression of internal defects due to the oxygen vacancies. Thus, reduction of the oxygen vacancies was thought to be a possible reason of increasing mobility with increasing partial pressure for the crystalline alloys. To further investigate the role of the reduction of internal defects, $(\text{In}_x\text{Ga}_{1-x})_2\text{O}_3$ alloys were deposited on sapphire substrate with a Ga_2O_3 buffer layer. The homoepitaxial buffer layer successfully increased the mobility of the crystalline alloys consistent with reducing the internal defects.

1. INTRODUCTION

Silicon has become the most widely used semiconductor, with a bandgap of 1.1 eV and other features that make it appropriate for most applications. Silicon belongs to the periodic table's group IV elements, and one of its main advantages is that it is affordable, mechanically strong, and non-toxic, making it ideal for producing a wide range of devices with good electrical properties. Scaling has made it possible to produce high density tiny transistors on a single piece of silicon. This increase in density has resulted in the current information technology boom [1]. However, one of the drawbacks of Si is that it has a narrow bandgap, making it only viable for devices with small breakdown fields, limiting its utility to high-power and high-temperature applications. Another downside of Si is that it is an indirect semiconductor, which limits its use in optoelectronics [2]. Other direct bandgap materials, such as the III-V system, are excellent for efficient opto-electronic devices like LEDs and lasers. For power devices, materials with a larger bandgap and a higher breakdown voltage are preferable to Si [3], [4]. For high power, high breakdown devices: SiC, GaN, and more recently Ga₂O₃ are being studied.

Semiconducting materials with high electrical breakdown and thermal conductivity are required for high power devices. To accomplish these features, scientists are looking into wide-bandgap binary, ternary, and their alloys. Breakdown voltage is inversely related to the bandgap's exponential power, which may be written as $E_c = \alpha(E_g)^n$, where E_c is the breakdown voltage, E_g is the bandgap, α is the rate at which holes and electrons ionize, and n is between 2 and 2.5 [5]–[7]. Also, the conductivity of the intrinsic semiconductor is significantly influenced by a material's band gap. Wide

bandgap semiconductors can therefore be used to achieve magnitudes of higher breakdown voltages with relatively thin layers, improving device scalability.

Wide bandgap semiconductors are semiconductors that allow devices to operate at significantly greater voltages, frequencies, and temperatures than typical semiconductor materials like silicon and gallium arsenide. Narrow-bandgap materials, such as Si, have bandgaps in the range of 1 to 1.5 electron volts (eV), whereas wide-bandgap materials have bandgaps in the range of 2 to 4 eV. As a result, wide-bandgap devices may function at significantly higher temperatures, up to 300°C with high power. Wide-bandgap semiconductors, such as silicon carbide (SiC) and gallium nitride (GaN), can lower switching losses, boosting efficiency, and can operate in harsher conditions, higher voltages, and switching frequency. In addition to emitters and detectors, direct wide-bandgap materials are used in ultraviolet electronics.

High-quality SiC and GaN substrates are too expensive for bulk manufacturing of power devices. The full potential of these alloys has not yet been realized due to a shortage of high crystal quality substrates, which causes dislocation and grain boundaries in the device structure. To get around this constraint, new materials are necessary [8]. Gallium oxide (Ga_2O_3) is a novel oxide semiconductor with a bandgap of 4.9 eV, which is higher than GaN and SiC [9]. Both thermally and chemically $\beta\text{-Ga}_2\text{O}_3$ is the most stable crystal structure among the five crystal forms of Ga_2O_3 . Recent developments made it possible to produce high-quality single crystal $\beta\text{-Ga}_2\text{O}_3$ substrates using melt-growing techniques such as the Czocharalski process, vertical Bridgman method, floating zone, and edge defined film-fed growth procedures [10]–[13]. Wide bandgap

semiconductors (WBG) have several uses in the field of power electronics, as shown in Figure 1.1.

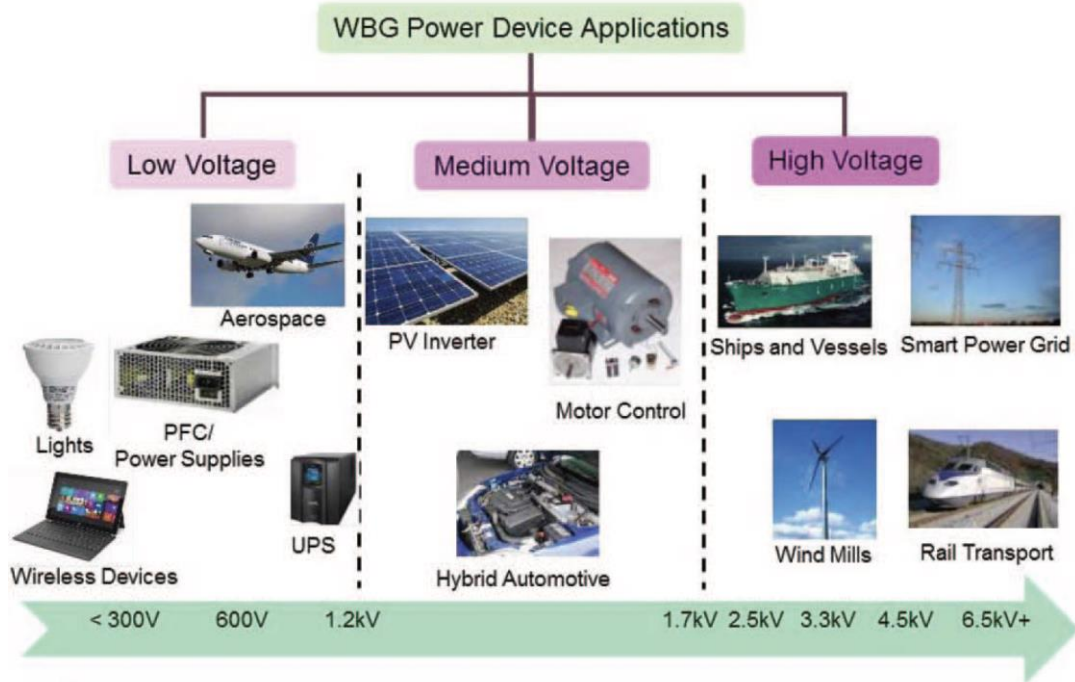


Figure 1.1: Applications of WBG for power electronics [10].

Ga_2O_3 is transparent to deep ultraviolet light and conductive. It is also employed as a transparent conductive oxide (TCO) layer. TCOs are electrically conductive materials with low visible light absorption. The Baliga figure of merit (BFOM) measures a material's appropriateness for a power device. BFOM refers to a vertical electronic device's lowest specific on-resistance, making $\beta-Ga_2O_3$ a good candidate for low-loss, high-voltage switching applications like high-breakdown Schottky diodes and field-effect transistors [13]. Additionally, the conductivity of Ga_2O_3 can be altered from an insulator to a conductor by altering the doping concentration and constructing heterostructures [14], [15]. According to reports, the alloys of Ga_2O_3 combined with In and Al exhibit bandgaps in the range of 3.5–8.6 eV, which is particularly effective for creating UV

detectors [16]–[18]. Bandgap engineering using heterostructures is the next phase towards developing high performance electronic devices because it enables modification of system's electrical and optical properties. Therefore, understanding the impact of growth parameters on the optical and electrical properties of these heterostructures is of paramount importance for the next generation of wide bandgap device technology.

The aim of the first part of this thesis is to study $(\text{In}_x\text{Ga}_{1-x})_2\text{O}_3$ structures grown on c-plane sapphire using pulsed laser deposition. For this, 25% In will be incorporated for the $(\text{In}_x\text{Ga}_{1-x})_2\text{O}_3$ thin films, and the impact of growth parameters such as substrate temperature and oxygen pressure on the structural and electrical properties (mobility and conductivity) of the thin films will be investigated. Crystalline structure and quality will be investigated using x-ray diffraction (XRD), electrical properties such as mobility and conductivity will be investigated by physical property measurement system (PPMS) using Van der Pauw Hall measurement technique, thickness of the thin films will be measured by ellipsometry, and the surface properties along with reason of change in mobility as a function of the growth condition will be determined by x-ray photoelectron spectroscopy (XPS). In the second part of this thesis, $(\text{In}_x\text{Ga}_{1-x})_2\text{O}_3$ thin films with 25% In concentration will be grown on c-plane sapphire with a buffer layer of Ga_2O_3 to investigate the effect of buffer layer in reduction of the defects in the thin films. Similar characterization techniques from the first part will be performed and a comparative analysis will be provided.

2. LITERATURE REVIEW

2.1 Crystal Structure of β -Ga₂O₃

Ga₂O₃ primarily forms five types of polymorphs denoted by α , β , γ , δ , and ϵ . α -Ga₂O₃ has a rhombohedral corundum crystal structure while γ , δ , ϵ have cubic, cubic, and hexagonal bixbyite crystal structure, respectively. The only form that can be created from the melt is β -Ga₂O₃, which is the most thermodynamically stable compared to the other polymorphs [9]. High temperatures generally cause other polymorphs to change into the β form [19]. With lattice constants of $a = 12.2 \text{ \AA}$, $b = 3.0 \text{ \AA}$, and $c = 5.8 \text{ \AA}$, β -Ga₂O₃ has a monoclinic crystal structure and is a member of the C2/m space group. Table 2.1 provides information about the phases of gallium oxide, including composition, reciprocal space group, and lattice characteristics.

Table 2.1: Lattice parameters for all Ga₂O₃ polymorphs [9]

Phase	Composition (at % O)	Space Group	Lattice Parameters (nm, deg)
α - Ga ₂ O ₃	60	$R\bar{3}c$	$a = 0.49791$ $c = 1.3437$
β - Ga ₂ O ₃	60	$C2/m$	$a = 1.2214$ $b = 0.30371$ $c = 0.57981$ $\beta = 103.83^\circ$
γ - Ga ₂ O ₃	60	$Fd\bar{3}m$	$a = 0.822$
δ - Ga ₂ O ₃	60	$Ia\bar{3}$	$a = 1.0$
ϵ - Ga ₂ O ₃	60	$Pna2_1$	$a = 0.5120$ $b = 0.8792$ $c = 0.9410$

Ahman et al. [20] presented the most recent and precise analysis of the crystal structure of β -Ga₂O₃. The results, while marginally different from Konh and Geller's previously published data, are much more accurate [21]. An obvious c-centered

monoclinic cell with the space group $C2/m$ was revealed by the X-ray diffraction symmetry. Figure 2.1 below illustrates the monoclinic $\beta\text{-Ga}_2\text{O}_3$ crystal structure. The angle between lattice parameters a and c is $\alpha = \gamma = 90^\circ$ and $\beta = 103.8^\circ$.

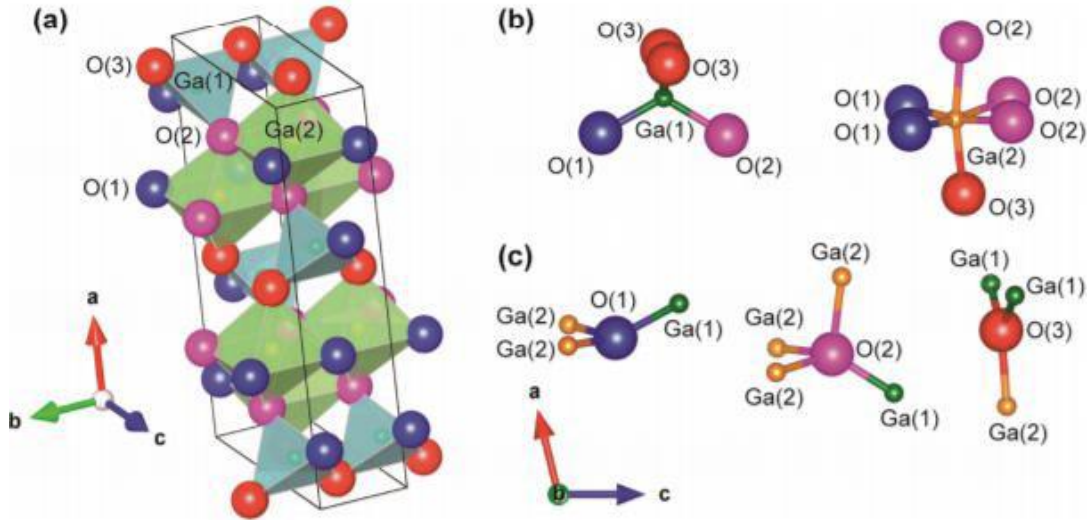


Figure 2.1: (a) Crystal structure of $\beta\text{-Ga}_2\text{O}_3$ showing O and Ga sites. (b) Ga (1) is the tetrahedral and Ga (2) is the octahedral site are the two-fold Ga sites, and (c) O (1) and O (3) are the two tri-coordination sites and O (2) is the four-coordination site [22].

$\beta\text{-Ga}_2\text{O}_3$'s unit cell consists of 8 Ga and 11 O atoms. The Ga and O sites are not equivalent. The two different Ga sites are the octahedral Ga (2) site, which has six oxygen atoms around it, and the tetrahedral Ga (1) site, which has four oxygen atoms surrounding it. The three oxygen sites that are also nonequivalent, with O (1) and O (3) being tri-coordinated and O (2) being four-coordinated [22], [23]. Due to its monoclinic structure, beta gallium oxide has a significant electrical breakdown potential for bandgap engineering, and phase transition by alloying with other elements further expands this potential for the development of new electrical and optical devices.

2.2 Material Properties of β -Ga₂O₃

β -Ga₂O₃ is the most researched polymorph of Ga₂O₃, as was previously noted, due to its availability and exceptional features. It is also the most stable form of all Ga₂O₃ polymorphs. The other polymorphic form transforms into the β form at a higher temperature, and the β form is chemically and thermally stable at higher temperatures. Due to its thermal stability, it is possible to produce single crystals and thin films using high-temperature techniques including melt growth and vapor phase epitaxy [24]. Since other types of crystals become unstable at higher temperatures, it is the only crystal structure that can be formed from the melt. It has been investigated for its possible use in opto-electronic devices due to its exceptional material characteristics. There are inconsistencies in the published data on several properties of β -Ga₂O₃, even though it is the polymorph that has been examined the most [9].

At room temperature, β -Ga₂O₃, naturally exhibits insulating properties. However, by altering the growth environment, it was possible to regulate the conductivity of the single crystal formed using the floating zone approach along the b axis from $<10^{-9}$ to $38 \Omega^{-1}\text{cm}^{-1}$ [25]. Additionally, it has been noted that β -Ga₂O₃ exhibits an insulating characteristic when doped with Mg [26]; while doping with the elements Sn, Ge, and Si increases the concentration of free electrons [25], [26].

When compared to other wide bandgap semiconductors, β -Ga₂O₃ performs poorly as a thermal conductor. Thermal conductivity varies in different directions because of crystallographic anisotropy. At room temperature, the results of a calculation of thermal conductivity using time domain thermos-reflectance (TDTR) showed that the highest thermal conductivity was $27\pm 2.0 \text{ W/mK}$ along [010] direction and the minimum

thermal conductivity was 10.9 ± 1.0 W/mK along [100] direction [27]. Using a laser flash method, the thermal conductivity was determined to be 21 W/mK in the [010] direction [26] and 13 W/mK in the [100] direction [28], which is considerably less than that of common semiconducting oxides. Thermal conductivities of large band gap semiconductors such as 4H-SiC (3.3 eV) and gallium nitride (3.4 eV) are 270 W/mK and 210 W/mK, respectively.

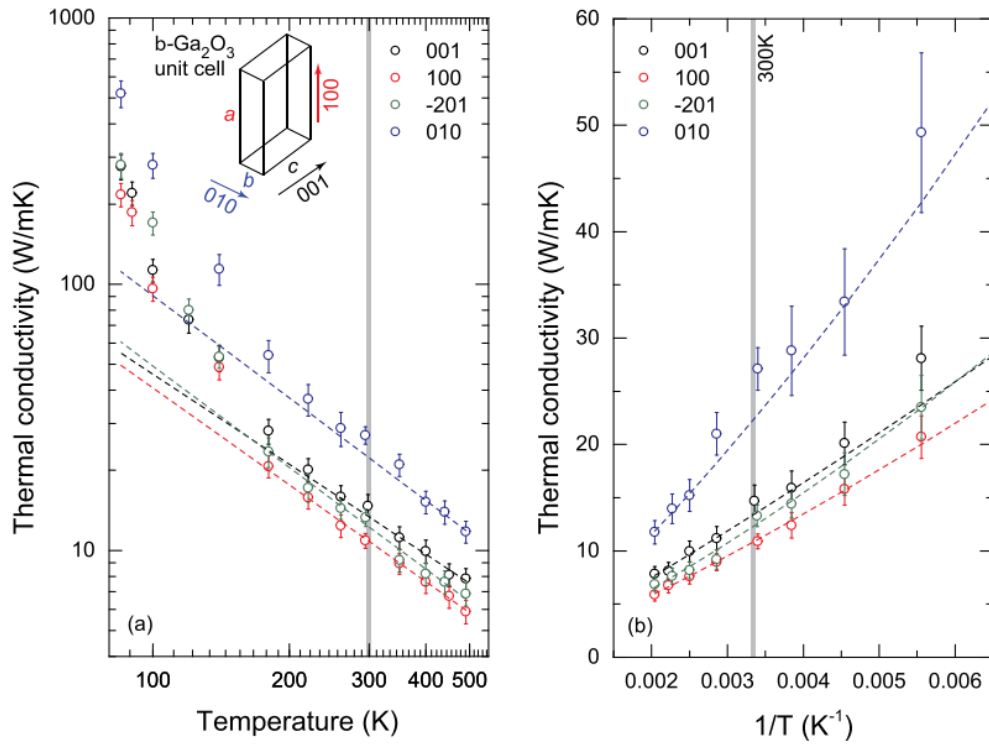


Figure 2.2: Thermal conductivity of β -Ga₂O₃ single crystal at different temperatures [27]

Heat dissipation can be a serious issue due to low thermal conductivity, which causes a device to heat up. Due to electron-phonon scattering at high temperatures, joule heating can cause a material's electrical transport characteristics to deteriorate by hundreds of degrees [27]. Therefore, efficient heat evacuation is crucial for electronic

devices to operate more effectively. Therefore, in order to use Ga_2O_3 efficiently, the material's reduced thermal conductivity needs to be addressed. The change in thermal conductivity of an EFG-grown single crystal of Sn-doped β - Ga_2O_3 at various temperatures is depicted in Figure 2.2. The thermal conductivity has a $1/T$ relationship at high temperatures, showing phonon-dominated heat transport [27]. Figure 2.2 illustrates that the thermal conductivity along the smaller lattice constant is larger.

Ga_2O_3 has a wide range of applications and uses including in opto-electronics and high-power devices due to its transparency up to the UV-C region and large band gap. β - Ga_2O_3 is effective and appealing for the power device application due to its wide bandgap and high electrical breakdown voltage, which can sustain high operating voltages. Ga_2O_3 has a very high Baliga Figure of Merit (3444) compared to GaN (870) and 4H-SiC (340) that indicates the possibility for power device use. The projected breakdown voltage is predicted to be 8 MVcm^{-1} , which is roughly three times more than either SiC or GaN. Conduction loss is also less due to the material's characteristics than it is in other semiconductor materials [24], [29]. So undoubtedly, Ga_2O_3 possesses high power applicability in power devices. A comparison of Ga_2O_3 's theoretical performance boundaries with those of the major semiconductors is shown in Figure 2.3.

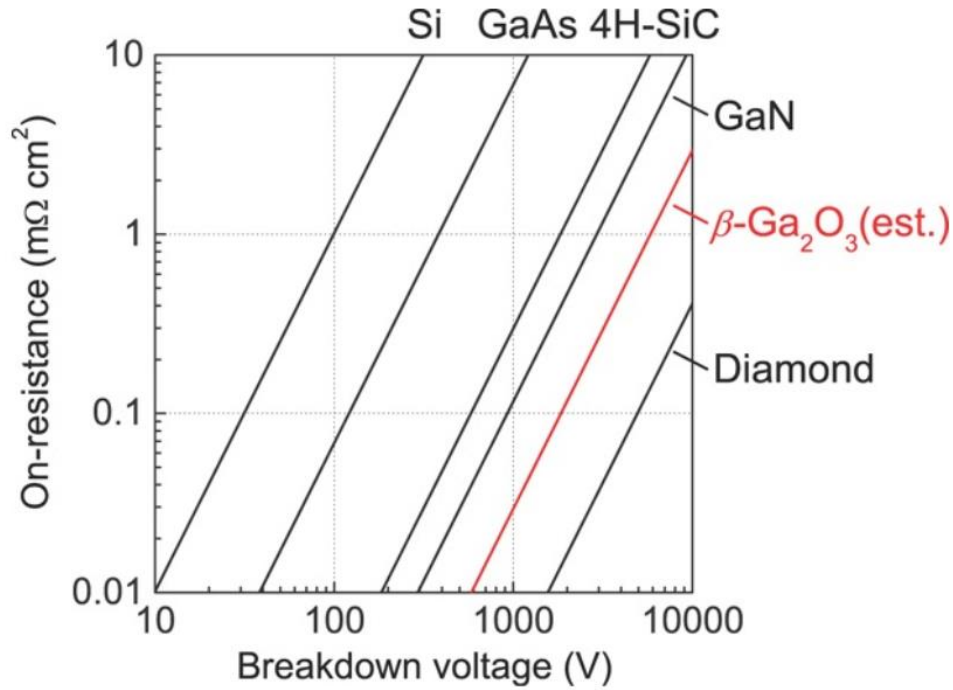


Figure 2.3: Theoretical ideal performance limits of β -Ga₂O₃ power devices against other major semiconductors [24]

The benefit of Ga₂O₃ in power device applications over current large bandgap semiconducting materials is the growth process available for mass manufacturing, in addition to its enormous breakdown voltage. SiC and GaN wafers are bulk synthesized from other nonefficient and costly growth methods since there are no melt growth methods available for their fabrication. The ability to create a single crystal of Ga₂O₃ using a variety of common melt growth techniques, however, gives it a significant advantage over SiC and GaN, especially for mass production [24], [29]. In table 2.2, the material characteristics of β -Ga₂O₃ are contrasted with those of common semiconductor materials.

Table 2.2: Comparison of β -Ga₂O₃ with other leading semiconductor materials [29].

Property	Si	GaAs	4H-SiC	GaN	Diamond	β -Ga ₂ O ₃
Bandgap, E_g (eV)	1.1	1.4	3.3	3.4	5.5	~4.9
Electron mobility, μ (cm ² V ⁻¹ S ⁻¹)	1400	8000	1000	1200	2000	300
Breakdown field, E_{br} (MVcm ⁻¹)	0.3	0.4	2.5	3.3	10	8
Relative dielectric constant, ϵ	11.8	12.9	9.7	9.0	5.5	10
Baliga's FOM, $\epsilon\mu E_b^3$	1	15	340	870	24664	3444

Ga₂O₃ has a large bandgap, making it an insulator at ambient temperature, but when it is synthesized under reducing conditions, it exhibits n-type conductivity. Oxygen vacancies are regarded as the cause of the n-type conductivity [25]. However, theoretical analysis utilizing the hybrid functional theory demonstrates that oxygen vacancies behave as deep donors with ionization energies of greater than 1 eV and cannot be the root cause of n-type conductivity. The likely reason of the electrical conductivity in unintentionally doped β -Ga₂O₃ is thought to be hydrogen [5]. Additionally, it has been suggested that the presence of silicon, a significant impurity in Ga₂O₃, may be the root cause of the n-type conductivity [29]. Additionally, it was shown that the growing environment and doping materials had a significant impact on the electrical characteristics of Ga₂O₃ [26]. A highly conductive Sn-doped Ga₂O₃ single crystal produced using the floating zone approach was described by N. Ueda et.al. [25]. It was found that adding group IV and group VII elements such as Ge, Si, Sn, F, and Cl increases the electrical conductivity of β -Ga₂O₃

because they act as shallow donors [5]. By doping with silicon, Ga₂O₃'s electrical conductivity increased by three orders of magnitude. Increasing the Si content caused the conductivity of Ga₂O₃ to change from 0.03 Ω⁻¹cm⁻¹ to 50 Ω⁻¹cm⁻¹. The free carrier concentration increased with Si concentration by over two orders of magnitude, from 10¹⁶ to 10¹⁸ cm⁻³, even though mobility was around 100 cm²V⁻¹s⁻¹ [14]. It was reported that, mobility of single crystal β-Ga₂O₃ grown by Czocharlski method is dependent on various scattering mechanism. Where the high temperature electron mobility was limited by phonon scattering the low temperature electron mobility was limited by impurity scattering [30]. Similar investigation was found on another study where it was reported that the electron mobility of bulk Ga₂O₃ substrates at high temperature is limited by polar optical (PO) phonon scattering [31]. In contrast, insulating behavior is exhibited in Ga₂O₃ with Mg doping. The single crystals of gallium oxide produced using FZ [32] and CZ [26] technology displayed enhanced resistance.

There is ongoing debate over Ga₂O₃'s p-type conductivity. Ga₂O₃ has not yet been reported to have good hole conduction. Theoretical calculations revealed that the valence band is flat, which indicates a higher effective mass for holes and makes p-type conductivity challenging [5], [33]. Based on I-V measurements, it was claimed that nitrogen-doped Ga₂O₃ nanowires had p-type conductivity, although neither the carrier concentration nor the mobility were provided [34]. Additionally, theoretical modeling demonstrated that nitrogen does not contribute to p-type conductivity because it functions as a shallow acceptor near the top of the valence band [35]. The self-localization of holes caused by the ionicity of metallic oxides has also been claimed to make p-type conductivity in β-Ga₂O₃ impossible. Despite effectively introducing a positive hole

through doping, it localizes on a single oxygen atom and is unable to move within the crystal lattice [36], [37].

2.3 Crystal Structure of In₂O₃

There are numerous polymorphs of indium oxide (In₂O₃), but the stable forms are cubic bixbyite ($Ia\bar{3}$, no.206) and rhombohedral ($R\bar{3}c$, no. 167) [38]. In addition to these polymorphs, the orthorhombic ($Pbcn$, no.60) phase is produced under high pressures and temperatures (8–9 GPa, 600–1100°C). However at room temperature, it largely transforms into the rhombohedral phase [39]. Table 2.3 displays the crystal structure parameters for these phases.

Table 2.3: Lattice and positional parameters for different phases of In₂O₃ [40]

Compound and space group	Unit cell (Å)	Atom	Wyckoff site	x	y	z
c-In ₂ O ₃	$a=10.1170$	In1	8b	0.25000	0.25000	0.25000
$Ia\bar{3}$	$a=10.1170$ $a=10.1170$	In2 O	24d 48e	0.46650 0.39085	0.000 0.15435	0.25000 0.38140
rh-In ₂ O ₃	$a= b=5.4814$	In	12c	0.0000	0.000	0.35720
$R\bar{3}c$	$c = 14.4998$	O	18e	0.96367	0.33333	0.58330
o-In ₂ O ₃	$a = 7.9295$	In	8d	0.11483	0.74607	0.02627
$Pbcn$	$b=5.4821$ $c = 5.55898$	O1 O2	8d 4c	0.85114 0.0000	0.61188 0.03792	0.09552 0.25000

This study will concentrate on In₂O₃'s cubic phase alloy with Ga. Two different types of indium atoms and one different type of oxygen atom occupy the 8b, 24d, and 48e

Wyckoff positions, respectively, in the cubic structure of indium oxide with a lattice value of 10.1170 \AA [40]. The b and d sites are two distinct indium locations where indium atoms are found in the middle of a warped cube with six corners occupied by oxygen atoms and two corners with oxygen vacancies [41]. As illustrated in figure 2.4, the vacancies in the b site are situated diagonally across the cube, while those in the d site are situated diagonally along a face. The unit cell contains 80 atoms which include 8 and 24 of these b and d site cations respectively [8].

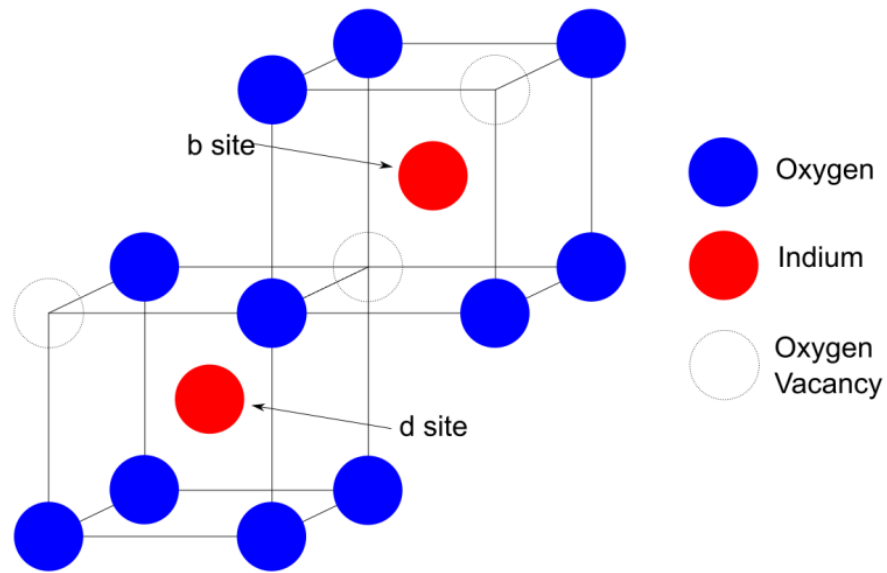


Figure 2.4: Crystal structure of cubic bixbyite In_2O_3 with the b and d sites [8].

2.4 Material Properties of In₂O₃

In₂O₃ has an optically determined bandgap of 3.75 eV [42], while other researchers have suggested that it may be closer to 2.9 eV [43]. For possessing conductive carriers resulting from intrinsic donor defects, In₂O₃ can be described as an n-type semiconductor [44]. Additionally, according to Agoston *et al.* [45], indium oxide has a high carrier concentration and is an efficient conductor even without doping with impurities but only if it is formed in an environment with low oxygen levels. According to reports, the carrier concentration ranges between 10¹⁷ and 10²⁰ cm⁻³, and as the oxygen pressure increases during growth, the carrier concentration decreases [46]. The most popular type of indium oxide for use in conducting electrical current is indium tin oxide (ITO), which has a resistance of just 7.7x 10⁻⁵ ohm-cm [38].

2.5 Alloy of (In_xGa_{1-x})₂O₃

Bandgap engineering is important for heterostructure device applications. Two materials with differing bandgaps combine to form heterostructures. The high bandgap range (3.7-4.9 eV) of (InGa)₂O₃ covering the wavelength range of 253-335 nm makes it a potential material for semiconductor optoelectronic devices. This range of wavelengths is in the ultraviolet (UV) spectrum, making it possible to employ the alloy in photodetectors, high electron mobility transistors (HEMTs), and UV optoelectronic devices. Because of the wide bandgap and anticipated high electric breakdown voltage, β-Ga₂O₃ based high power HEMTs appear promising. In and Ga were chosen to create the alloy because they both have the same electronic structure and belong to the same column III element group. The fabrication conditions determine the anticipated crystal structure of the alloy. With respect to their respective cubic and monoclinic crystal forms, In₂O₃

and Ga_2O_3 are projected to phase separate depending on the In content. $(\text{InGa})_2\text{O}_3$ can be used as transparent conducting oxide (TCO). Since it has a low absorption coefficient in the visible region, it can also be used for coating transparent substrates such as plastic, glass, and semiconductors [47], [48].

This alloy can be created using several techniques, including MBE and PLD. According to research by Zhang et al. [49], $(\text{InGa})_2\text{O}_3$ film grown on sapphire (0001) at 500 °C by PLD over a range of compositions has been demonstrated. It was discovered that mixed phases of the cubic and monoclinic structures exist for indium contents between 0.16 and 0.33. The monoclinic phase was the only one to be observed with indium content lower than 0.16. The polycrystalline cubic structure with XRD peaks indicating the (222) and (400) orientations were identified for indium content between 0.33 and 0.56. Indium content above 0.83 revealed the single crystal cubic structure.

Oshima and Fujita [50] explored the phase separation between cubic In_2O_3 and monoclinic Ga_2O_3 using MBE in their investigation. The samples were produced with a monoclinic Ga_2O_3 buffer layer at 800 °C and 1.1×10^{-7} Torr Ga beam equivalent pressure on double-polished c-plane sapphire (0001) substrates. XRD scans showed the cubic structure at an indium composition of 43%, however because of the buffer layer, it was not evident at what indium composition the film became fully single crystal cubic. For high indium compositions, they noticed a decrease in crystallinity. Additionally, it was asserted that low temperature growth was required to reduce phase separation.

In a study by Wenckstern [51], PLD was used to produce thin films of $(\text{In}_x\text{Ga}_{1-x})_2\text{O}_3$ on a two-inch diameter c-plane sapphire wafer. Ball milling, pressing, and sintering at temperatures of 1600°C for 12 hours and 1350°C for 72 hours, respectively, were used

to create the In_2O_3 and Ga_2O_3 targets. The ceramic targets were split in half, and one semicircular In_2O_3 and one semicircular Ga_2O_3 target were used to create a single target. The background oxygen pressure was 10^{-5} mbar, and the growth temperature was around 650°C . According to XRD spectra, the thin film possessed a monoclinic crystal structure for low In concentrations ($x < 0.15$), while the cubic bixbyite phase was found for high In levels ($x > 0.8$). Beside the monoclinic and cubic phases, the crystalline phase of rhombohedral $(\text{InGa})_2\text{O}_3(\text{II})$ was seen in the intermediate alloys.

In a study by Fabi Zhang and Qixin Guo [52], $(\text{InGa})_2\text{O}_3$ films were created by pulsed laser deposition at room temperature on (0001) sapphire substrates. With a laser energy of 225 mJ, a frequency of 1Hz, and a deposition rate of 40 minutes, the films were produced at an oxygen pressure of 0.1 Pa (0.00075 Torr). The target had indium contents of 0.2, 0.3, 0.5, and 0.7. Up to a nominal indium content of 0.3, the films preserved the (201) oriented monoclinic structure of $(\text{InGa})_2\text{O}_3$, but the films with nominal indium contents of 0.5 and 0.7 exhibit a cubic structure (222) oriented diffraction patterns along with the monoclinic phase. Additionally, it was noted that the (-402) peak position of monoclinic and (222) peak position of cubic structures of $(\text{InGa})_2\text{O}_3$ films gradually migrated toward a lower angle with increasing nominal indium content, indicating an increase in the lattice constant. It had not been possible to clearly discern the coexistence of the two structures.

Sheng-Po Chal et al. [53] in their research investigated the influence of different partial pressure on the fabrication of InGaO ultraviolet photodetectors. Here IGO films of thickness 200nm were deposited on quartz substrate by RF magnetron sputtering. The films were deposited at room temperature using an IGO ceramic target where the atomic

ratio of In and Ga was 9:1. During the process, the gas flow ratio of O₂/Ar was varied from 0%-20% and the pressure was fixed at 5 mtorr. The XRD results showed that with increasing oxygen pressure, the crystalline properties were improved. It was also shown that at low oxygen partial pressure, because of the presence of a large number of subgap states, the devices work in the photoconductive mode. But with the increase of partial oxygen pressure, the deficiencies in the IGO crystal lattice were filled by the oxygen in the chamber which led to reduce the vacancies in the films.

3. GROWTH AND CHARACTERIZATION TECHNIQUES

3.1 Deposition Technique

3.1.1 Pulsed Laser Deposition (PLD)

PLD is a physical vapor deposition (PVD) procedure that uses a high energy density laser radiation to ablate ceramic target pellets. This procedure involves performing the deposition in a vacuum chamber equipped with a heating system and gas inlets to regulate and adjust the deposition settings for a variety of thin film materials. Due to its stoichiometric transfer of composition from the target, PLD is considered by researchers to be one of the most promising growth technologies for achieving high quality epitaxial development of oxide thin films. Soon after the first ruby lasers were created in 1965, this procedure had already been put into practice. However, it took several years before the research labs were able to use this technology for the deposition of high-quality thin films, mostly because there were no high-energy lasers available. Epitaxial growth of the high-temperature superconductor at Bell Communication was what first sparked by the advent of PLD in 1986/1987 [54].

In a vacuum chamber, a ceramic target pellet is positioned close to a heated substrate. Cylindrical sintered pellets are used as targets. As the laser beam is incident on target, a plasma plume is created which is directed normal towards the substrate. The substrate is situated in front of target at a distance of a few cms away. It is very easy to tailor the content in the deposited films by changing the composition in target material. PLD is a promising technique for the deposition of high-quality films at growth temperatures in the range of 200°C–800°C. The crystalline quality of PLD grown thin films depends on various parameters such as laser energy, growth temperature and

growth pressure. A laser with a high energy density (here a KrF excimer laser with a wavelength of 248 nm) is focused on the target surface to ablate material that then forms a plasma plume. The particles of the plasma move towards the substrate where they can condense as a solid thin film. The schematic diagram of the PLD system is shown in figure 3.1.

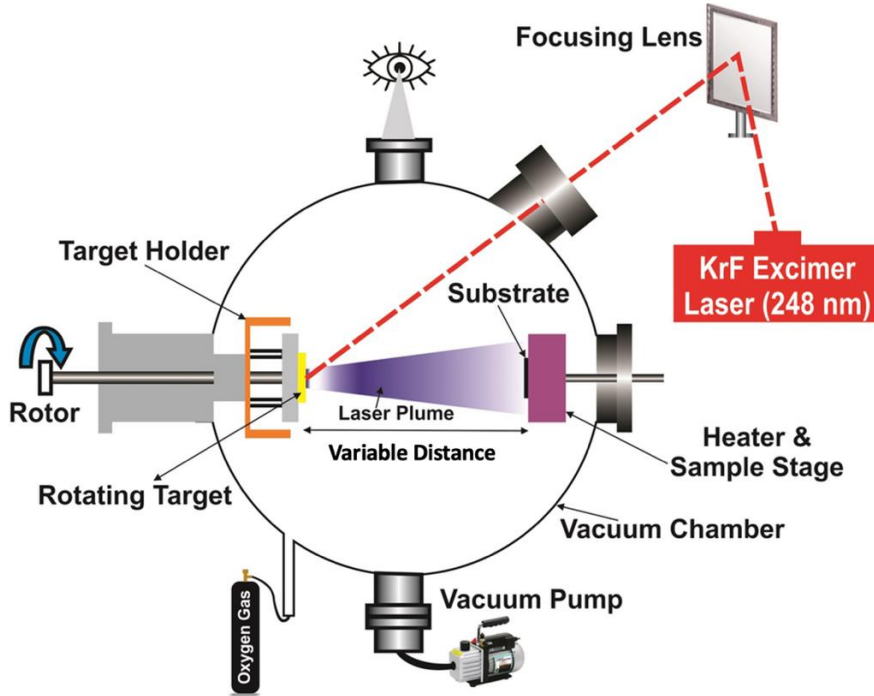


Figure 3.1: Schematic diagram of PLD system [55].

The laser is the most crucial component of the PLD system, and excimer lasers such as KrF (248 nm wavelength) and XeCl (308 nm wavelength) are typically utilized since most target materials need high energy densities (more than 1 J/cm^2) to effectively produce a plume from the target [56]. A separate Coherent excimer laser source (KrF) with a wavelength of 248 nm is used in the PLD system in Dr. Droopad's lab. Through a series of lenses and mirrors, the laser beam is guided to focus on the target materials at about a 45-degree angle. When the target material is ablated by high-power laser pulses, a

plasma cloud or plume is produced. The laser beam can be regulated to deliver a certain amount of power and pulses. The target material can then be transferred into the substrate in a stoichiometric manner enabled by the plume.

Oxygen flow and adjusting the turbo pump's speed can be used to modify the pressure during thin film deposition. Mass flow controllers (MFC) are used to regulate the gas inflow. Using a load lock chamber and a transfer arm, the substrate and the target can be inserted into the growth chamber. Typically, a combination of turbomolecular pumps and rough vacuum pumps maintains vacuum in both the load lock chamber and the main chamber.

A heater that can rotate 360 degrees and reach temperatures of up to 1000°C is located inside the sample stage. Different sizes and shapes of substrates can be used in the holder (max substrate size is 2 inches in diameter). The substrate is frequently rotated during growth to guarantee homogeneous heating and deposition. By adjusting the target and substrate distance using the sample stage, the ideal distance can be experimentally attained. The target itself is rotated to preserve stoichiometric growth and maintain craterless ablation of the target disks. The target holder contains a total of six target disks, and their positions can be altered during or before growth using stepper motor controllers.

Contrasted with other physical vapor deposition processes, PLD is a relatively straightforward deposition method but offers a huge number of benefits. When the target material is transferred stoichiometrically in a particular chamber setting, high-quality films are produced with fewer control parameters. A high degree of flexibility is provided by the MFC-controlled background gases and a wide range of temperature variations, which can serve to provide a better knowledge of the growth process for improving

growth recipes. Furthermore, throughout the deposition process, the target materials can be varied, greatly simplifying the creation of complicated thin film heterostructure. PLD not only enables researchers to examine the impact of the thin film's compositional change by varying the substrate's temperature and oxygen partial pressure, but also contributes to morphological optimization by varying the laser's repetition rate and power [57].

3.1.2 Target Preparation

Target preparation is crucial for the PLD deposition system since the deposition material comes from the ablation of a target. Ceramic sintering is used to prepare the targets. To manufacture the intended target with a specific mole fraction, the first step is to measure high purity oxide powder or, for alloys, to measure many oxide powders while taking into consideration their atomic weight percentages. A ball milling machine is used to combine the powders for 30 to 40 minutes. The powder is then placed in a mold with a particular diameter and pressed within for 24 hours at 300 degrees Celsius and 15000 pounds per square inch to form a solid ceramic disk. The disk is then sintered in a high-temperature furnace with flowing Ar gas for 12 to 20 hours at 1000°C.

3.2 Characterization

3.2.1 X-ray Diffraction (XRD)

XRD is an effective method for examining the structural characteristics of materials at the level of lattice plane distances. It depends on electromagnetic radiation's interference, diffraction, and scattering on the periodic atomic structure of the crystal lattice. The crystalline structure of a deposited layer can be ascertained using constructive interference in a non-destructive manner. For a specific crystalline structure, waves

interacting in the atomic plane of a material will produce constructive and destructive interference with the arranged atoms. This interference can reveal structural characteristics such as crystalline phases, defects, unit cell dimensions, lattice parameters, etc. [58]. Since the typical lattice plane distances are in the range of a few Å, the used electromagnetic radiation must have a wavelength in this range. The radiation of choice in this situation is X-rays, which can be created by a standard X-ray tube using electrons accelerated up to many tens of keV towards a cathode metal. The used distinctive X-ray spectrum is produced by deceleration within the metal and excitation of electrons from core levels, followed by filling of these levels by electrons from outer shells. Most research equipment typically uses Cu K radiation with $\lambda \approx 1.54 \text{ \AA}$. Highly monochromatized synchrotron radiation is used in more advanced techniques.

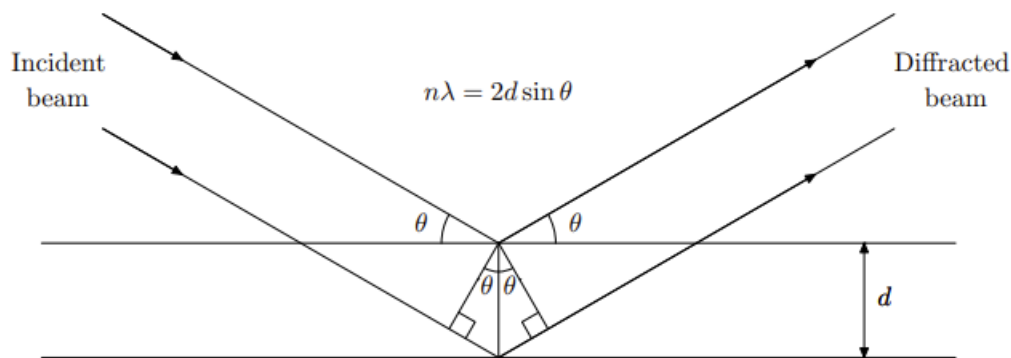


Figure 3.2: Schematic diagram demonstrating Bragg's law [59].

The Bragg equation, which serves as the foundation of X-ray diffraction, can be calculated using a straightforward model by the constructive interference of two X-rays scattered over two lattice planes separated by d_{hkl} . Bragg's law is expressed as $n\lambda = 2d_{hkl} \sin \theta$ where n is an integer defining the diffraction order, λ is the wavelength of the

X-rays, θ is the incident angle, and d_{hkl} is the lattice spacing between diffracting planes. Figure 3.2 explains Bragg's Law in a crystal plane [17].

By sweeping the sample surface in a variety of 2θ angles, it is feasible to obtain all of a lattice's potential diffraction directions. If a crystal's inter-planar space is unstrained, it will display its distinctive diffraction pattern. The inter-planar spacing of the $\{hkl\}$ lattice planes can alter in a strained crystal lattice plane due to tensile and compressive strain, which can shift the peak of the diffraction pattern. Thus, strain inside the crystal structure can be determined by monitoring peak shift and quantitatively quantifying inter-planar separation. The quantitative analysis of inter-planar space and strain is performed in an orthogonal coordinate system.

In this study, the effect of various parameters on the generated $(\text{In}_x\text{Ga}_{1-x})_2\text{O}_3$ thin films is examined using a Rigaku SmartLab XRD equipment. The Cu K source ($\lambda=1.540562 \text{ \AA}$), the goniometer stage on which the sample is placed, and the Hybrid Photon Counting detectors (HPC) are used in the Rigaku SmartLab XRD device. Numerous diffraction techniques can be used with the apparatus, which normally runs at 40 kV and 44 mA.

3.2.2 Ellipsometry

Ellipsometry is an incredibly accurate, non-destructive method of measuring optical reflectance with unmatched capabilities for thin film metrology. Ellipsometry can offer details on each of these factors because the composition, thickness, conductivity, and porosity of thin films all have an impact on their optical characteristics. The basic idea behind ellipsometry is that the amplitude ratio of two perpendicularly polarized beams can be used to determine how the polarization of light reflected from the sample

surface has changed. In this method, electromagnetic radiation is produced by a light source and linearly polarized by a polarizer before passing through a quarter-wave plate or other optional compensator and irradiating the sample. After reflection, the radiation travels via an optional compensator and a second polarizer (analyzer) before being detected [60]. Figure 3.3 illustrates the basic ellipsometry configuration.

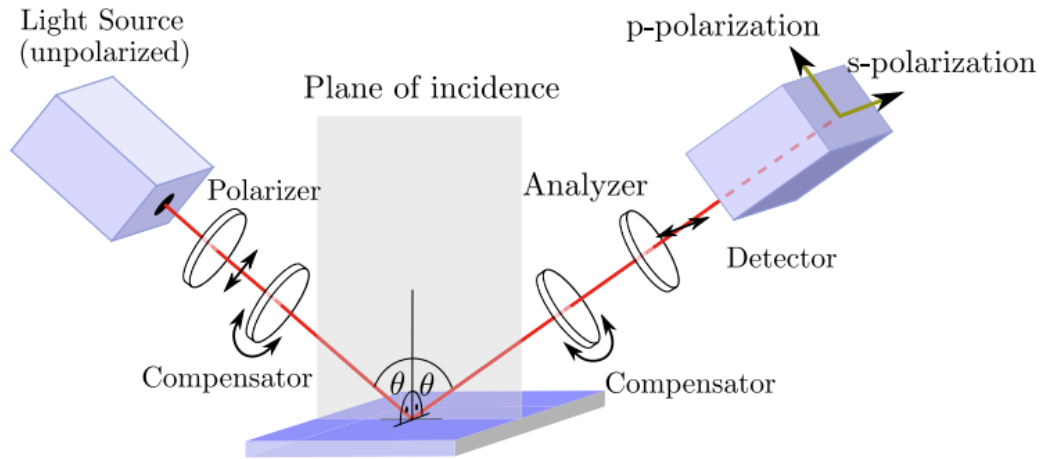


Figure 3.3: Configuration of ellipsometry [61]

The light's polarization state can be broken down into its s and p components when it strikes the sample. The p component oscillates parallel to the plane of incidence while the s component oscillates perpendicular to the plane of incidence and parallel to the sample surface. Equation 1 is used to determine the complex reflectance ratio(ρ) using the amplitudes of the s and p components after reflection and normalization to their initial value, indicated by r_s and r_p :

$$\rho = \frac{r_p}{r_s} = \tan(\psi) e^{i\Delta} \quad (1)$$

where $\tan(\Psi)$ is the amplitude ratio upon reflection, and Δ is the phase difference [62].

$$\tan(\psi) = \frac{\left(\frac{E_p}{E_s}\right)_{Reflected}}{\left(\frac{E_p}{E_s}\right)_{Incident}} \quad \text{and } \Delta = \Delta_p - \Delta_s$$

Here E_p and E_s are the electric field of p and s polarized light, respectively. The optical constants and sample thickness are derived by applying an appropriate model analysis to the data and finding the two parameters Ψ and Δ , and that best match the experimental data. The best estimate is where the Root Mean Squared Error (RMSE) is the lowest, which is provided by the fit estimation [63].

The thickness, roughness, and optical characteristics of the samples are examined in this study using an M-2000 Woollam ellipsometer. For a spectral range of 200nm to 800nm, measurements are made at three incidence angles of 55°, 65°, and 75°.

3.2.3 Physical Property Measurement System (PPMS)

A DynaCool physical property measurement system (PPMS) is used to study the magnetic and electrical transport properties of materials in an environment where the magnetic field and temperature are well-controlled. These types of materials are typically in bulk, thin film, and powder form. The equipment provides several measurement capabilities for solid samples without the need for any liquid cryogenes. The PPMS DynaCool system uses a single two-stage Pulse Tube cooler to cool both the superconducting magnet and the temperature control system, providing a low vibration environment for sample measurements. This also comes standard with an integrated cryopump that is used to pump the sample space to a vacuum of $<10^{-4}$ Torr. The Dynacool PPMS system used in this study provides a temperature range of 4K-300K and a magnetic field of up to 9 Tesla to conduct the temperature dependent Hall measurement and analysis.

The technique of Hall measurement is used to ascertain a material's electrical properties, such as sheet resistance, resistivity, mobility, and carrier concentration. Due to the simplicity and convenience of the geometry, the van der Pauw approach is widely utilized in industry [1]. The van der Pauw geometry employed in this study is shown in Figure 3.4.

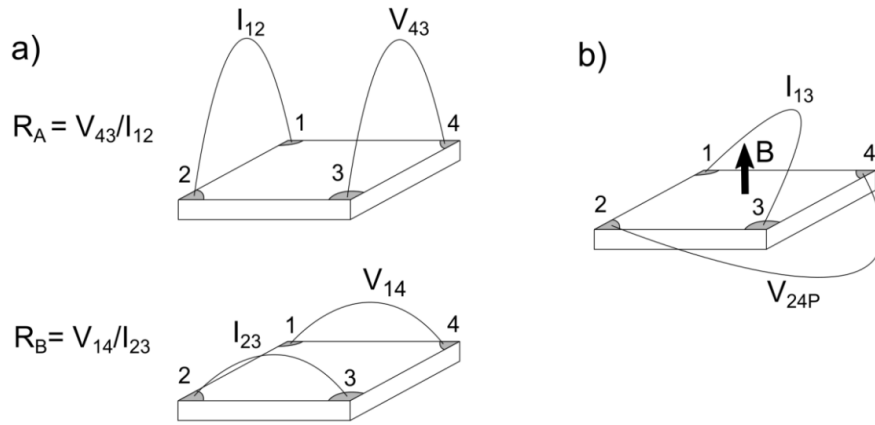


Figure 3.4: Illustration of the sample geometry for Van der Pauw (a) resistivity (b) Hall measurement [64].

Resistance measurements (R_A , R_B) are taken in accordance with the formulas depicted in figure 3.4(a). A more accurate value for the two characteristic resistances, now known as R_V and R_H , is obtained by averaging reciprocal measurements of R_A and R_B . The characteristic resistances are determined by averaging the results of the four resistance measurements after the voltage and current connections are swapped to further improve the measurement. The relationship between the sheet resistance (R_S) and two characteristic resistances is shown by the van der Pauw formula depicted in equation 2:

$$\exp\left(-\frac{\pi R_V}{R_S}\right) + \exp\left(-\frac{\pi R_H}{R_S}\right) = 1 \quad (2)$$

Solving this equation for R_S , the resistivity (ρ) can be found by equation 3:

$$\rho = R_S d \quad (3)$$

where d is the thickness of the sample.

The setup depicted in figure 3.4(b) is utilized to compute the Hall voltage. During the application of a constant positive (voltage- induced reference by subscript P) or negative (voltage-induced reference by subscript N) magnetic field (B) perpendicular to the sample, a constant current (I_{13}) is applied, and the voltage (V_{24P}) is monitored. The current I_{13} is a positive current produced between contact 1 and contact 3 while the voltage V_{24} is the voltage difference across those contacts ($V_4 - V_2$). The net voltage for each measurement (the difference between the measured voltage with a positive and negative magnetic field (e.g., $V_{24} = V_{24P} - V_{24N}$)), is then averaged to give the Hall voltage (V_H). With the Hall voltage known, the carrier concentration (n) can be derived using equation 4:

$$n = \frac{IB}{q|V_H|} \quad (4)$$

Upon finding the sheet resistance and carrier concentration, the mobility (μ) of an n-type semiconductor can be found by equation 5:

$$\mu = \frac{1}{qnR_S} \quad (5)$$

3.2.4 X-ray Photoelectron Spectroscopy (XPS)

X-ray photoelectron spectroscopy is a surface-sensitive analytical method that bombards a material's surface with x-rays and measures the kinetic energy of the photoelectrons that are released. XPS is one of the most widely used methods for analyzing the chemical composition of the surface in thin films. With the aid of this technique, solids' compositions, band structures, and band alignments can all be identified. In a setting of ultrahigh vacuum, x-rays are used for the measurements. The

sample is exposed to soft x-rays with energies below 6 keV, and the kinetic energy of the released electrons is measured. When all of the x-ray energy is transferred to a core level electron, a photoelectron is produced. The binding energy of the released electrons determines the kinetic energy of the core electrons, which is measured by the detector. The kinetic energy can be utilized to identify the element because the core levels of each element are distinct. Typically, soft x-rays such as Al K α serve as x-ray sources (1486.6 eV) [65]. The kinetic energy released can be expressed as equation 6:

$$K.E. = h\nu - (B.E. - \phi) \quad (6)$$

Here, K.E. and B.E. are the kinetic energy of the electron and binding energy in the shell, respectively, $h\nu$ is the x-ray energy, and ϕ is the work function of the spectrometer. An excited, ionized state of the atom results from the removal of the core electron. The atom attempts to enter a state of relaxation by releasing energy. For qualitative investigation, XPS can also be utilized to find Auger electrons [66]. The atomic species present on the material's surface can be precisely described by the detection of electrons. The XPS processes that take place when an X-ray incident on a sample surface are shown in figure 3.5 below:

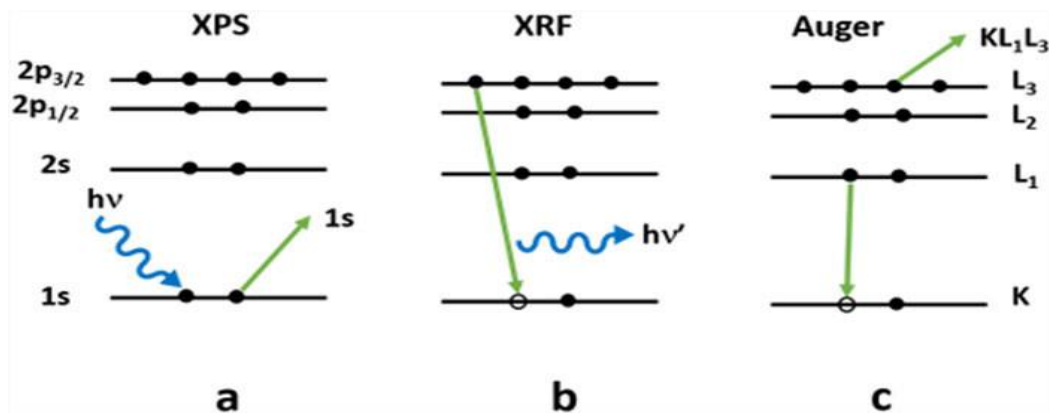


Figure 3.5: Processes that result from X-ray bombardment of a surface include (a) emission of a photoelectron, (b) x-ray fluorescence, and (c) emission of an Auger electron [66]

The NEXSA XPS was used for the XPS measurement in this study, and the Avantage analytic program was used for the analysis. It uses a monochromatic Al $K\alpha$ x-ray source operating at 15 kV and 14 mA, with an energy of 1486.6 eV. Peak deconvolution was carried out by employing gaussian line shapes to identify components that comprise chemical interaction of the properties of the elements on the surface. A Shirley backdrop was employed during the analysis to match the data. In order to neutralize the charge on insulators or semiconductors, the flood gun remained constantly active when using XPS to probe. Each time, the XPS did a three-level depth profiling on the as-grown samples to get rid of surface impurities.

4. RESULT AND DISCUSSION

4.1 Experimental

The first step of the deposition process is to prepare a target containing the correct percentage of In with β -Ga₂O₃ powder. High purity gallium oxide powder (99.999%) with indium content with molar ratio of In/(In+Ga) equating 0.25 is mixed to create (In_xGa_{1-x})₂O₃ targets. As indium concentration below 16% exhibited monoclinic phase whereas indium concentration between 16%-33% exhibited mixed phases of cubic and monoclinic structures in (In_xGa_{1-x})₂O₃ thin films [49], and mixed phase of the alloy exhibits conductivity, an alloy with 25% In concentration was used in this study to investigate the electrical properties of the (In_xGa_{1-x})₂O₃ thin films. In the PLD chamber, the (In_{0.25}Ga_{0.75})₂O₃ thin films are grown on (0001) oriented c-plane sapphire stoichiometrically, so the ratio of In and Ga in the film should not change. The sapphire substrate was cleaned with acetone and isopropanol in an ultrasonic bath and then rinsed in deionized water. The ablation of the target onto the substrate was carried out using the krypton fluoride (KrF) laser with a 248nm wavelength. The pulse repetition rate was fixed at 5Hz, and a total of 5000 pulses was used to deposit on the substrate with 300 mJ beam power. To investigate the influence of substrate temperature and partial oxygen pressure on the structural and electrical properties of (In_{0.25}Ga_{0.75})₂O₃ thin films, the temperature was initially varied from 400°C to 700°C. Later, the temperature was fixed, and oxygen pressure in the chamber was varied from 5x10⁻² to 1x10⁻² to investigate the impact of oxygen pressure. The target and the substrate were rotated for uniform film distribution, and the distance between them was fixed at 5cm. Finally, β -Ga₂O₃ / (In_xGa_{1-x}

x) $_2$ O $_3$ heterostructure was deposited on c-plane sapphire, and the effect of homoepitaxial buffer layer on defect reduction of the thin films was investigated.

4.2 Impact of Growth Parameters

The high-resolution XRD 2θ - ω scans for In concentration= 25% in the (In $_x$ Ga $_{1-x}$) $_2$ O $_3$ (IGO) thin films were taken in order to determine the impact of substrate temperature and oxygen partial pressure on the crystal quality. Figure 4.1 shows the XRD 2θ - ω spectra for $x = 25\%$ IGO thin films grown at different substrate temperatures (400°C - 700°C) while keeping the oxygen partial pressure fixed at 5×10^{-2} torr. The x-ray spectra show the formation of a mixture consisting of (-201) oriented β -(In $_{0.25}$ Ga $_{0.75}$) $_2$ O $_3$ thin films and (222) planes of cubic structure grown at temperatures above 500 ° C. The film exhibits amorphous crystallinity below this temperature due to not having the proper nucleation energy. The diffraction peaks fall within the {-201} family of planes for β -Ga $_2$ O $_3$, and the reflection planes (-201), (-402), (-603), and (-804) correspond to the 2θ angles around 18.81°, 38.65°, 58.57°, and 82.97° respectively. Additionally, the diffraction peaks correspond to the (222) and (444) planes of cubic In $_2$ O $_3$ at 30.34 ° and 63.25 ° respectively. The c-sapphire substrate reflection planes are indicated with (0001) and (0006) at the diffraction angles of 20.52° and 41.56° respectively. Crystallinity increases with increasing temperature as the lowest full width half maxima (FWHM) of monoclinic and cubic phases 0.42086 and 0.47749 respectively were obtained at a growth temperature of 700 ° C. The degraded crystallinity at low growth temperature can be attributed to having insufficient energy for the adatoms to migrate and nucleate on the surface. Hwang *et al.* [67] also reported an amorphous phase at low substrate temperature but increased crystallinity was obtained after annealing.

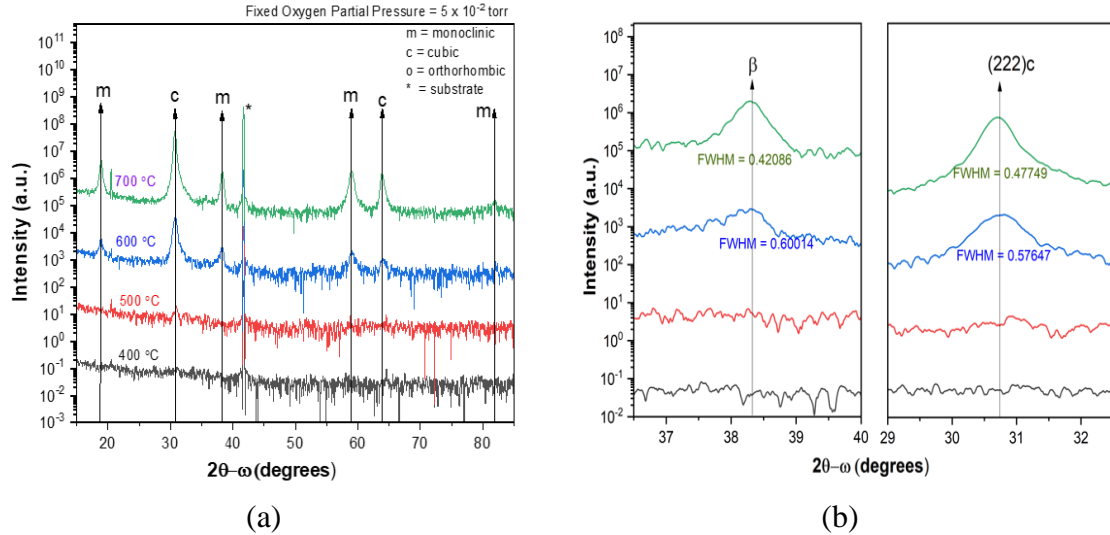


Figure 4.1: (a) XRD measurement of $(\text{In}_{0.25}\text{Ga}_{0.75})_2\text{O}_3$ grown at different substrate temperatures and (b) corresponding FWHM measurement of monoclinic and cubic plane.

In the next step, to investigate the effect of partial oxygen pressure on the grown films, the temperature was fixed, and the oxygen flow was varied to change pressure from 1×10^{-3} - 5×10^{-2} torr. The fixed substrate temperature was chosen to be 600 °C and 500 °C to make a comparison between the amorphous and crystalline films and investigate their effect on mobility and conductivity which will be discussed later. Figure 4.2 exhibits XRD $2\theta-\omega$ spectra of $(\text{In}_{0.25}\text{Ga}_{0.75})_2\text{O}_3$ thin films with varying oxygen pressure (1×10^{-3} - 5×10^{-2} torr) during PLD deposition at a fixed substrate temperature of 600 °C. Even though PLD deposition is stoichiometric, the oxygen atmosphere during growth can significantly impact the crystallinity of the grown thin film. Park et al. [68] also reported crystallization characteristics of IGO thin films with varying oxygen pressure. Their research showed that increasing oxygen pressure increases the crystallinity to a certain extent. In addition, Kaleemulla et al. [69] showed that crystallinity of In_2O_3 films increased with higher oxygen partial pressure. From figure 4.2, it is clearly seen that a second phase beside the monoclinic phase is present

at low pressure that is 1×10^{-3} torr. This phase can be attributed to both the ϵ -phase and the κ -phase; thus, further investigation is required to differentiate between them.

Usually, the ϵ -phase and the κ -phase are reported besides the β -phase for $(\text{In}_x\text{Ga}_{1-x})_2\text{O}_3$, these phases are typically present with the β -phase using a small amount of Sn into the target material. The Sn in gallium oxide alloys promotes higher amounts of Ga to move into the octahedral position avoiding excess formation of suboxides [70]–[73].

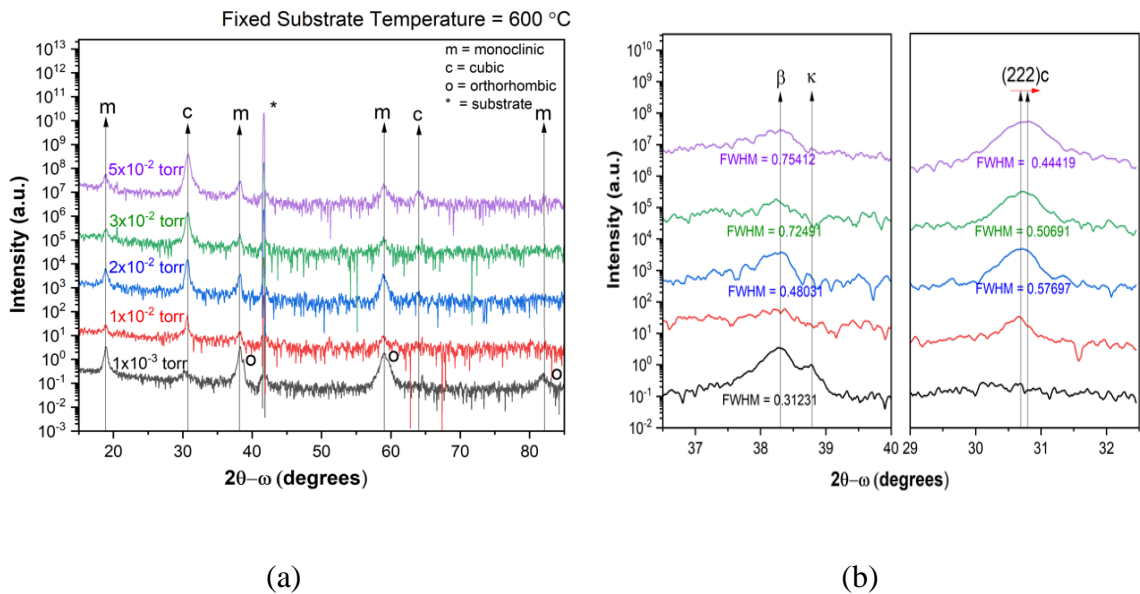


Figure 4.2: (a) XRD measurement of $(\text{In}_{0.25}\text{Ga}_{0.75})_2\text{O}_3$ grown at different oxygen inflow with fixed substrate temperature of 600°C and (b) corresponding FWHM measurement of monoclinic (β) and cubic (c) plane.

Above 1×10^{-3} torr pressure, the film showed both monoclinic and cubic phases and the diffraction angles were the same as figure 4.1. The intensity of the cubic phase seemed to increase with increasing pressure and the lowest FWHM value for the cubic phase was obtained at the highest pressure. The monoclinic phase behaved differently as the lowest FWHM value for the monoclinic phase was obtained at low pressure which is

1×10^{-3} torr. Also from this figure, it can be shown that the cubic phase shifted to a higher 2θ angle with the increase of pressure. As discussed above that for cubic phase the intensity increased with increased pressure, improved crystal quality results in a denser structure of IGO film. At higher oxygen partial pressure, increased scattering of ablated species by the molecules of oxygen gas can suppress volatile GaO suboxide evaporation. The right shift of the cubic peak thus may be attributed to the suppress of the evaporation of volatile Ga_2O species from the substrate surface [72]. The reason behind this peak shift requires further investigation.

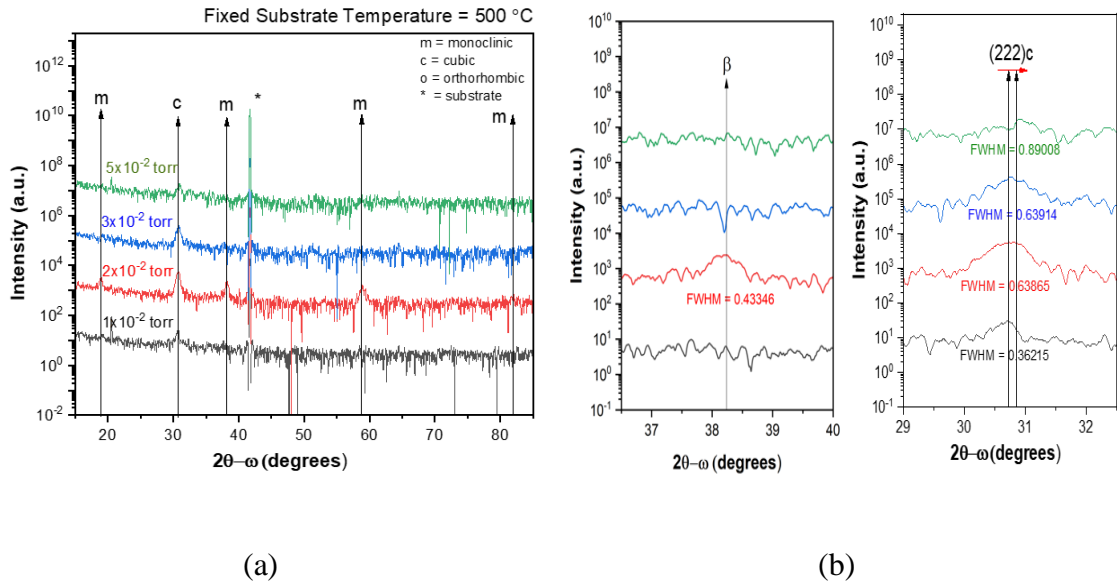


Figure 4.3: (a) XRD measurement of $(\text{In}_{0.25}\text{Ga}_{0.75})_2\text{O}_3$ grown at different oxygen inflow with fixed substrate temperature of 500°C and (b) corresponding FWHM measurement of monoclinic (β) and cubic (c) plane.

Figure 4.3 illustrates the impact of different oxygen partial pressure (1×10^{-2} - 5×10^{-2} torr) during the growth of $x = 25\%$ $(\text{In}_x\text{Ga}_{1-x})_2\text{O}_3$ thin films at a substrate temperature of 500°C. Here oxygen partial pressure seems to have less effect on the crystallinity. For all the pressures, the films exhibited an almost amorphous phase as the peak intensities

for the peaks were very small. No additional phase was observed beside the monoclinic and cubic phases. Here the cubic peak was also observed to shift to higher 2θ angle which can be attributed to evaporation of volatile Ga_2O species from the substrate surface.

Spectroscopic ellipsometry was used to further investigate the properties such as thickness and surface roughness of the as-grown $(\text{In}_x\text{Ga}_{1-x})_2\text{O}_3$ films. The measurement was carried out at room temperature for wavelengths ranging from 200 nm to 1000 nm and three incident angles of 65° , 75° and 85° . The ψ and Δ values for the entire interval of wavelengths were used to investigate the physical properties. A substrate and as-grown film stack with roughness were used as the model for the analysis, and the model was then fitted for ψ and Δ values for the entire wavelength interval with minimum mean square error (MSE). Table 4.1 and Table 4.2 shows the extracted data from ellipsometry showing the thickness and roughness of the as-grown thin films for different substrate temperatures (fixed chamber pressure at 5×10^{-2} torr) and different oxygen partial pressures (fixed substrate temperature at 600°C and 500°C) respectively.

From table 4.1, we can see that the deposition temperature has a significant impact on the growth of the IGO thin films. The thickness of the grown films seems to be decreasing with increasing temperatures, and the roughness is also reducing in a similar trend. This can be attributed to the growth quality and crystallization of the thin film. The crystal quality gradually improves when IGO is deposited with a higher substrate temperature (shown in the XRD study from figures 4.1). Improved crystal quality results in a denser structure of IGO film, resulting in lower thickness and improved roughness. Another reason for lower thickness with increasing temperatures can be attributed to

evaporation of volatile sub oxide species from the substrate surface at elevated temperatures [74], [75].

Table 4.1: Materials properties of $(\text{In}_x\text{Ga}_{1-x})_2\text{O}_3$ at a fixed pressure of 5×10^{-2} torr and variable substrate temperatures

Substrate Temperature	Thickness (nm)	RMS Roughness (nm)
400°C	200.35	4.93
500°C	187.40	4.88
600°C	174.88	3.92
700°C	151.23	2.95

On the contrary, at lower substrate temperatures, the film becomes amorphous and less evaporation of Ga_2O occurs at a lower temperature. This leads to higher thickness and an increase in the surface roughness in the as-grown IGO films. Yuan et al. [76] also reported similar phenomena in their study on aluminum gallium oxide thin films grown by pulsed laser deposition system.

Table 4.2: Materials properties of $(\text{In}_x\text{Ga}_{1-x})_2\text{O}_3$ at two fixed temperatures of 600°C and 500°C with variable oxygen inflow

Substrate Temperature	Chamber Pressure	Thickness (nm)	RMS Roughness (nm)
600°C	1×10^{-2} torr	150.45	2.85
	2×10^{-2} torr	161.38	3.05
	3×10^{-2} torr	170.74	3.29
	5×10^{-2} torr	174.88	3.92
500°C	1×10^{-2} torr	156.57	2.93
	2×10^{-2} torr	168.09	3.51
	3×10^{-2} torr	175.08	3.67
	5×10^{-2} torr	187.40	4.88

Similar to the variations with temperatures, the chamber pressure variance caused by different oxygen partial pressure during growth also impacts the thickness and roughness of the grown thin films (table 4.2). At higher oxygen partial pressure, increased scattering of ablated species by the molecules of oxygen gas can suppress volatile Ga₂O suboxide evaporation, and the re-sputtering effect can diminish the growth thickness [72].

For all the samples either varying pressure or substrate temperature the thickness was within 150-200nm. This thickness value obtained is used to calculate the mobility and resistivity of the thin films which will be discussed below.

In order to investigate the effect of growth parameters on the electrical properties of (InGa)₂O₃ thin films, the mobility and resistivity of the grown films using different growth conditions were determined and investigated. The resistivity and mobility were calculated by implementing Van der Pauw Hall measurement technique using PPMS. Before proceeding to Van der Pauw Hall measurement system, the resistivity and mobility values of all the samples were collected from the Bio-Rad Hall measurement system at room temperature. No resistivity and mobility data were found for the samples grown at chamber pressure below 2×10^{-2} torr from the Bio-Rad Hall measurement system. So, it can be said that, to get conductive samples, the chamber pressure should be at or above 2×10^{-2} torr. The lowest value of resistivity for the sample grown at 600°C substrate temperature was 8.6×10^{-2} Ω-cm which was found at the highest chamber pressure (5×10^{-2} torr). At room temperature, for the sample grown at 500°C substrate temperature, the lowest value of resistivity (7.8×10^{-2} Ω-cm) was measured at the chamber pressure of 3×10^{-2} torr. After that the samples grown at various oxygen pressure (2×10^{-2} - 5×10^{-2} torr) and at two fixed substrate temperature (600°C and 500°C respectively) were

selected for the temperature dependent Hall measurement process. To implement the van der Pauw Hall measurement technique, the samples were first cut into small square shape and In contact was placed on the four corners of the samples by soldering. In PPMS, the temperature was swept from 4K-300K with a fixed magnetic field of 0.5 Tesla. The current was fixed in such a way that for the whole range of temperature, the I-V curve remain linear indicating ohmic contact. This temperature dependent Hall measurement system provides the value of sheet resistance and Hall coefficient from which resistivity and mobility values can be calculated. Figure 4.4 shows the temperature vs resistivity for various oxygen pressure at substrate temperature of 600°C and 500°C respectively.

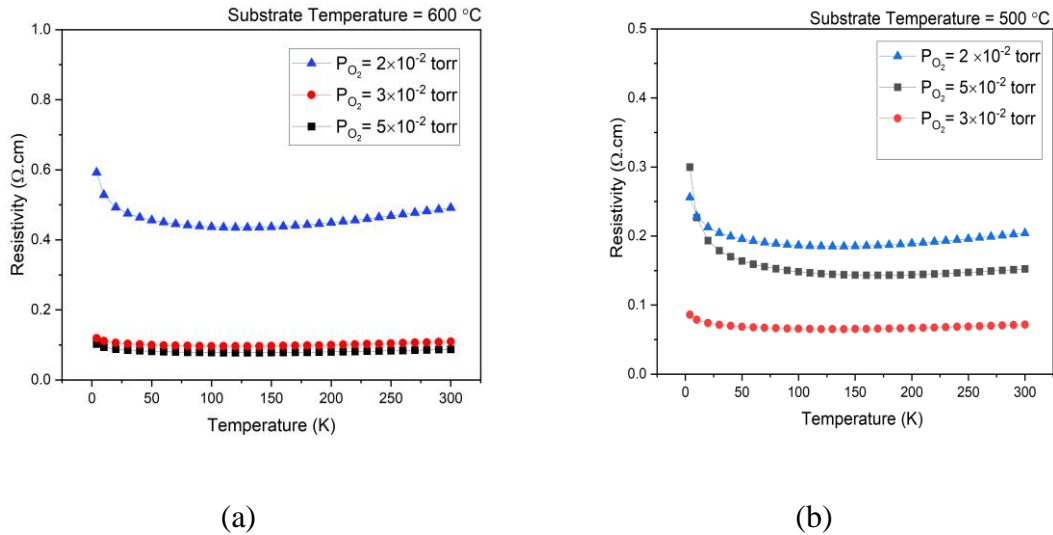


Figure 4.4: Temperature Vs Resistivity measurement of the samples grown at various oxygen pressure and at fixed substrate temperature of (a) 600°C and (b) 500°C.

From figure 4.4(a), for the samples grown at substrate temperature 600°C, the resistivity decreases with increasing oxygen pressure. However similar trend was not found for the films grown at substrate temperature 500°C. From figure 4.4(b), the lowest resistivity was found at chamber pressure of 3×10^{-2} torr. The lowest values obtained here

at RT were almost similar to the result collected from Bio-Rad Hall measurement system. From the XRD analysis of figure 4.1, it was discussed that the substrate temperature needs to be above 500°C to achieve crystallinity and at substrate temperatures below or at 500°C the films exhibited amorphous quality. For the crystalline films, the reduction of resistivity with increasing pressure may be attributed to the suppression of defects in the films with increasing chamber pressure. But for the amorphous films, no such defects are present. Therefore, the pressure has no significant effect on the resistivity for these films. Further investigation is required to investigate the effect of pressure on resistivity for amorphous thin films.

The temperature vs mobility both for crystalline and amorphous films is shown in figure 4.5. The mobility gradually increased with the increase pressure for the crystalline phase that is shown in figure 4.5(a). Whereas pressure has no noticeable impact on the mobility for the amorphous films depicted in figure 4.5(b). As discussed above that due to not having defects, the resistivity of the amorphous films may not be affected by pressure variation. A similar explanation is applicable for the dependency of mobility on pressure variation for the films having amorphous phase. From the ellipsometry data, the thickness was found to be increasing with increasing pressure. So, from figure 4.5(a), it is evident that the mobility is increasing with the increase of thickness of the films. Also comparing the data between figures 4.5(a) and 4.5 (b), it is clear that the mobility of the amorphous films for any pressure is higher compared to that of crystalline films and the possible reason of this can be the improvement of thickness with reducing temperature. So, it can be attributed that mobility is proportional to the thickness of the films. Also, the presence of grain boundaries in crystalline films can have an impact on the mobility.

Grain boundaries being the interface between grains or crystallites are 2D defects in crystal structure which tend to decrease the mobility of the material. So, from this we can say that the absence of grain boundaries in the amorphous samples is the reason of increased mobility in the amorphous samples compared to the crystalline samples.

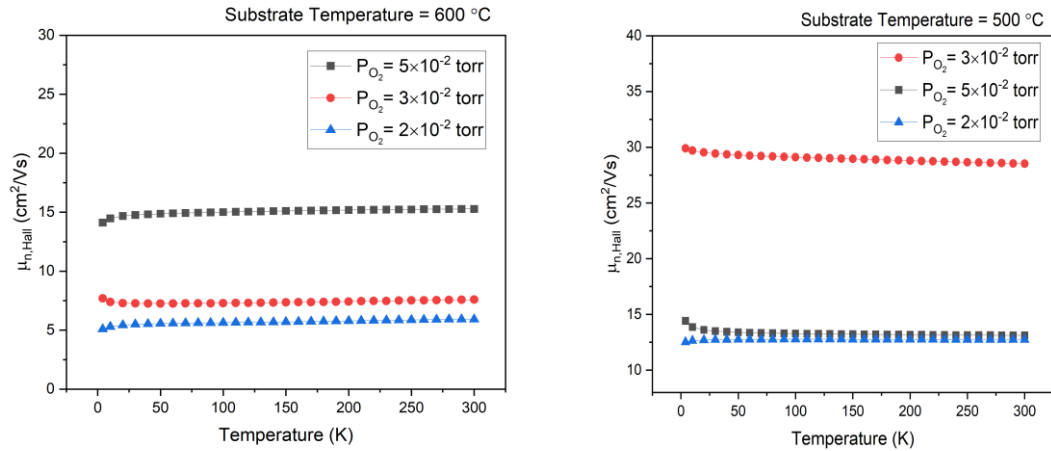
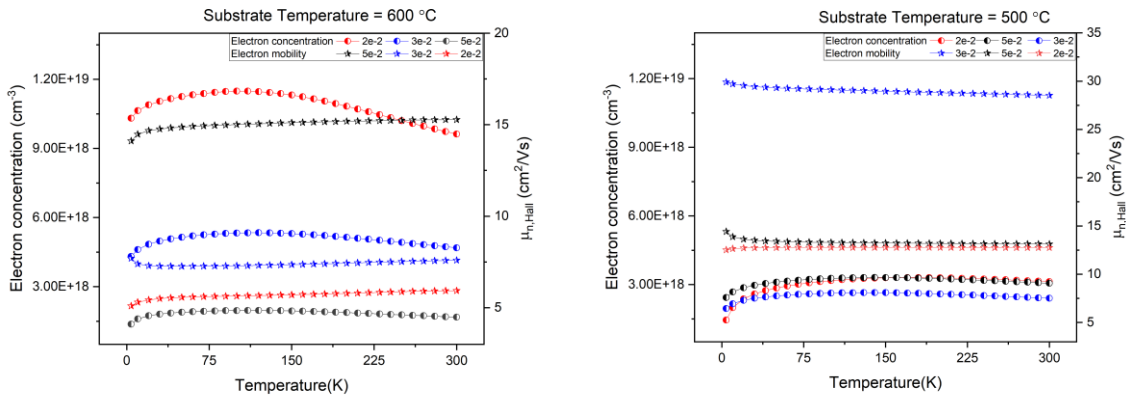


Figure 4.5: Temperature Vs Mobility measurement of the samples grown at various oxygen pressure and at fixed substrate temperature of (a) 600°C and (b) 500°C.

From the Bio-Rad Hall measurement system, the maximum mobility for the crystalline film was found to be 14.45 cm^2/Vs at chamber pressure of 5×10^{-2} torr and 27 cm^2/Vs was calculated at chamber pressure of 3×10^{-2} torr for the amorphous films. From the temperature dependent mobility values, the highest mobility values for both kind of films are found to be almost same as Bio-Rad Hall measurement data. The scattering mechanisms limiting mobility could not be investigated here as the maximum temperature limit for the PPMS is 300K. Higher temperature range and additional impurity doping is required to analyze the effect of scattering mechanisms on mobility.

Figure 4.6 depicts temperature vs carrier concentration and mobility plot for both crystalline and amorphous films where the lines with circular symbol represent the carrier

concentration and the lines with star symbol represent the mobility. From this plot, it can be seen that the samples with higher mobility have lower carrier concentration. The carrier concentration decreased with increasing partial oxygen pressure for the crystalline samples and amorphous samples exhibited lower carrier concentration compared to the crystalline samples.



(a) (b)
Figure 4.6: Temperature Vs Carrier Concentration and Mobility measurement of the samples grown at various oxygen pressures and at fixed substrate temperatures of (a) 600°C and (b) 500°C.

Finally, the surface characteristics of the as-grown thin films were investigated using X-ray photoelectron spectroscopy to explore the surface composition and chemical states of the (InGa)₂O₃ thin films. The carbon peak at 184.8eV was used as a reference peak to shift the spectrum to mitigate charging effects. The survey spectra showed gallium peaks, indium peaks, oxygen peaks, and a carbon peak. There were no other impurities visible from the spectrums. The In 3d region is chosen along with Ga 3d and O 1s to determine the oxidation states of the indium and gallium in the thin film and their effect on the change of mobility with increasing oxygen pressure.

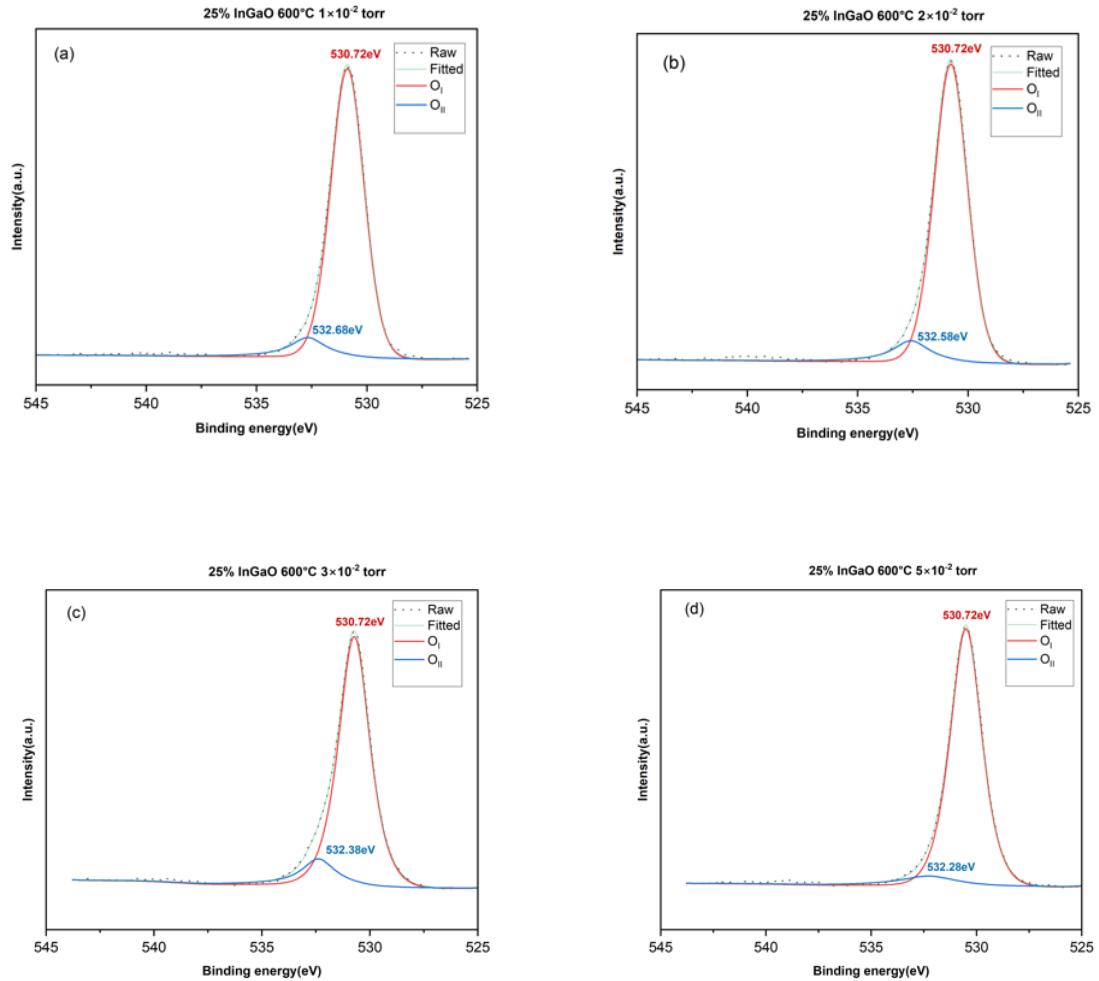


Figure 4.7: High resolution O 1s core level XPS spectra of $(\text{InGa})_2\text{O}_3$ for various oxygen partial pressure (a) 1×10^{-2} torr (b) 2×10^{-2} torr (c) 3×10^{-2} torr and (d) 5×10^{-2} torr respectively with a fixed substrate temperature of 600°C .

The O1s peak for $(\text{InGa})_2\text{O}_3$ thin films is presented in figure 4.7. The impact of partial oxygen pressure on the $(\text{In}_x\text{Ga}_{1-x})_2\text{O}_3$ thin films is investigated for $x = 25\%$. The growth conditions, such as temperature, laser power, pulse repetition, and pulse number were kept constant at 600°C , 300mJ, 5Hz, and 5000 pulses, respectively. The chamber pressure was varied from 1×10^{-2} torr to 5×10^{-2} torr by varying oxygen inflow into the

chamber. Figure 4.7 (a) – (d) illustrates the deconvolution of O1s spectra of $(\text{InGa})_2\text{O}_3$ for different oxygen inflow into the chamber.

The O1s peak was deconvoluted into two peaks through a mixed Gaussian and Lorentzian fitting procedure. The lowest peak belongs to the lattice oxygen in crystalline $(\text{InGa})_2\text{O}_3$ is centered around 530.7 eV and denoted as O_I . The peak with the highest binding energy, centered around 532.5 eV, belongs to absorbed O_2 or oxygen vacancies of the thin film and denoted as O_{II} . With the increased oxygen inflow in the chamber, we can see that compared to O_I peak, the O_{II} peak shifted to a lower binding energy. The shift of the O_{II} peak to the lower binding energy was attributed to the reduction in oxygen vacancies [53], [77]. The proportional areas of the sub-peaks are also being affected. This suggests that the partial oxygen pressure alters the O1s bonding states. As oxygen vacancy state (O_{II}) in an oxide thin film is a matter of great importance, researchers used $\text{O}_{II}/\text{O}_{\text{total}}$ to quantitatively determine the level of oxygen vacancy-related defects [53], [78], [79]. Here, O_{total} is the sum of O_I , and O_{II} .

With the increase of oxygen inflow during growth, the $\text{O}_{II}/\text{O}_{\text{total}}$ is declining. This means that the excess oxygen in the chamber fills up the vacancies in the $(\text{In}_x\text{Ga}_{1-x})_2\text{O}_3$ crystal lattice. The reduction of the oxygen vacancies attributed to the suppression of the internal defects due to the oxygen vacancies which in turns increases the mobility [77], [80]. From the temperature vs mobility data, it was found that the highest mobility for the crystalline film was achieved at the highest chamber pressure which is 5×10^{-2} torr. And from the XPS O1s scan it is evident that, at 5×10^{-2} torr the binding energy of the O_{II} peak is the lowest. So, from this discussion it can be concluded that oxygen vacancy reduction

can be a possible reason for increasing mobility with oxygen partial pressure for crystalline samples.

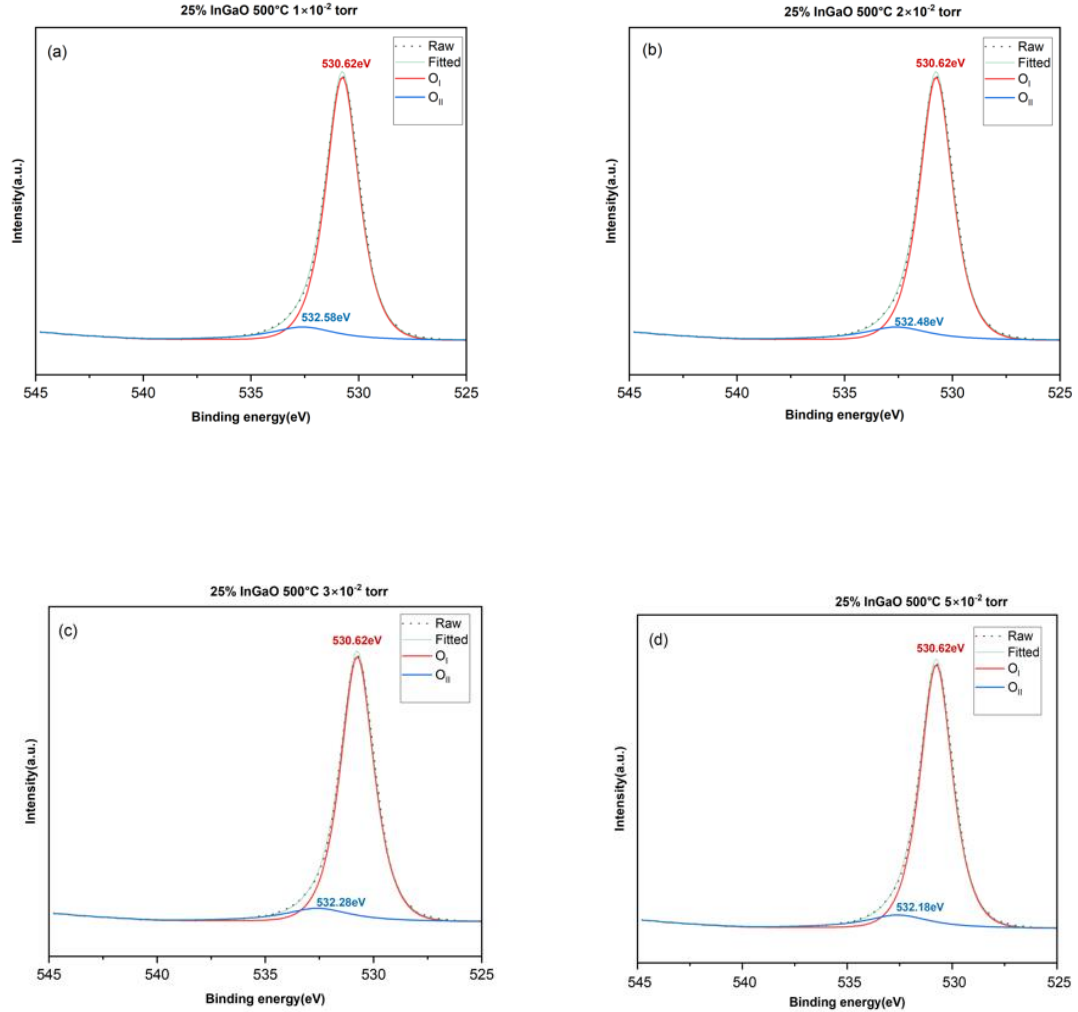


Figure 4.8: High resolution O 1s core level XPS spectra of $(\text{InGa})_2\text{O}_3$ for various oxygen partial pressure (a) 1×10^{-2} torr (b) 2×10^{-2} torr (c) 3×10^{-2} torr and (d) 5×10^{-2} torr respectively with a fixed substrate temperature of 500°C .

The impact of the partial oxygen pressure on the $(\text{In}_x\text{Ga}_{1-x})_2\text{O}_3$ thin films was depicted in figure 4.8 where the chamber pressure was varied from 1×10^{-2} torr to 5×10^{-2} torr by varying oxygen inflow into the chamber and substrate temperature was fixed at 500°C . Same as the previous analysis, with respect to the O_I peak, the O_{II} peak also

appears to shift to lower binding energy with increasing partial oxygen pressure . But the highest mobility for the samples grown at 500°C substrate temperature was found at the chamber pressure of 3×10^{-2} torr. For this, the shift of the O_{II} peak and reduction of oxygen vacancies cannot be attributed to the change in mobility for the amorphous films. Further investigation is required to find the reason of change in mobility for thin films having amorphous phase.

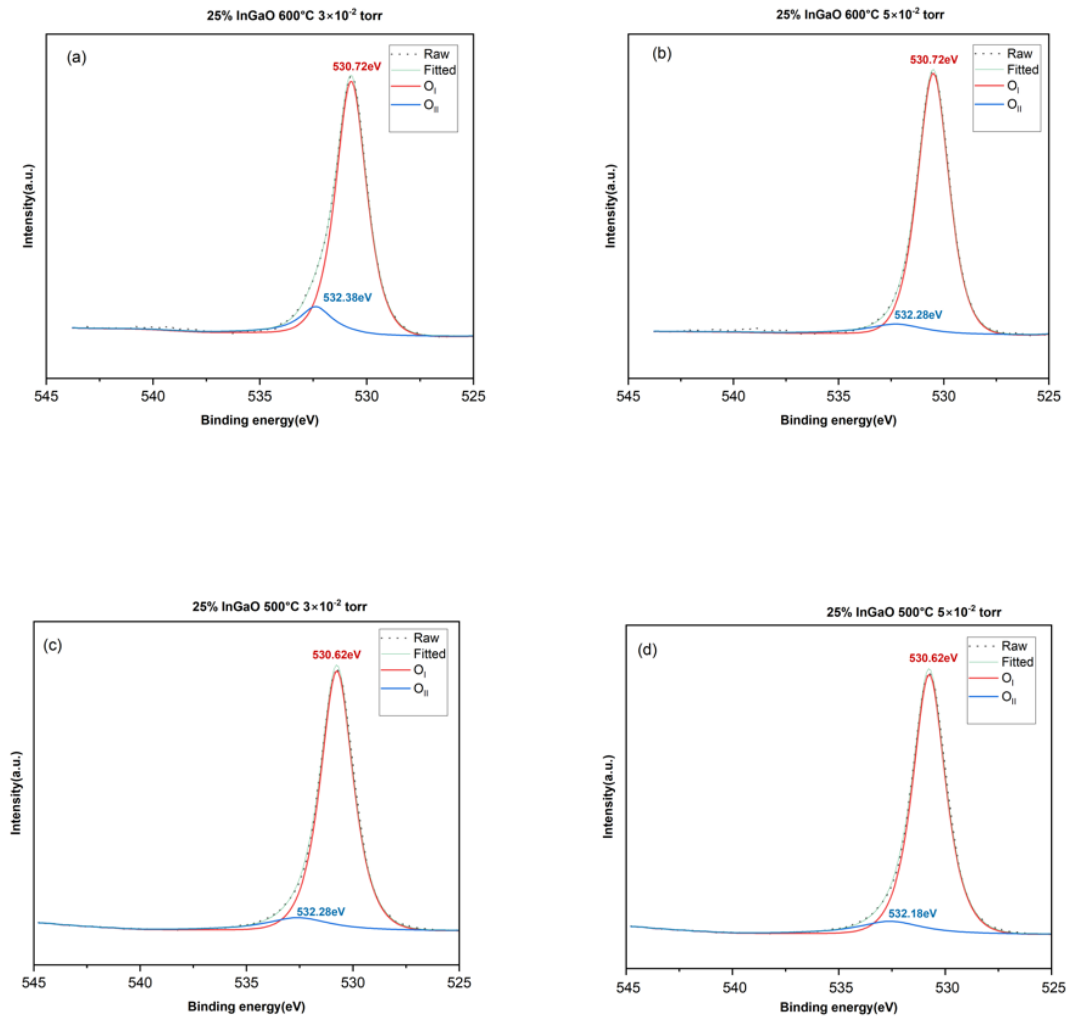


Figure 4.9: High resolution O 1s core level XPS spectra of (InGa)₂O₃ for various oxygen partial pressure (a) 3×10^{-2} torr (b) 5×10^{-2} torr with fixed substrate temperature of 600°C. (c) 3×10^{-2} torr and (d) 5×10^{-2} torr with a fixed substrate temperature of 500°C.

From the analysis of temperature vs mobility, the amorphous films were found to have higher mobility compared to the crystalline films. From the XPS O1s scan of both the films from figure 4.9, it is evident that, for the amorphous films, both the O_I peak and the O_{II} peak shifted to the lower binding energy compared to that of crystalline films. Also, the intensity of the O1s peaks is found to be less for the samples grown at 500°C substrate temperature compared to that of samples grown at 600°C substrate temperature. The reduction of the peak intensity was found to be a possible reason for reduction in oxygen vacancies [80]. So, both for the reduction of peak intensity and peak shift to the lower binding energy, the amorphous samples have higher mobility compared to the crystalline films.

Figure 4.10 shows the In 3d region to determine the oxidation state of indium. The peak is deconvoluted into two regions: In 3d_{3/2} at around 452 eV and In 3d_{5/2} at around 444 eV. From this figure, with increasing pressure, a shift of the In 3d peaks to the lower binding energy side is observed. This peak shift was attributed to the decrease of In oxidation state [77]. So, this phenomenon can also be attributed to the increase of mobility with increasing partial pressure for the crystalline films as shown in figure 4.4(a).

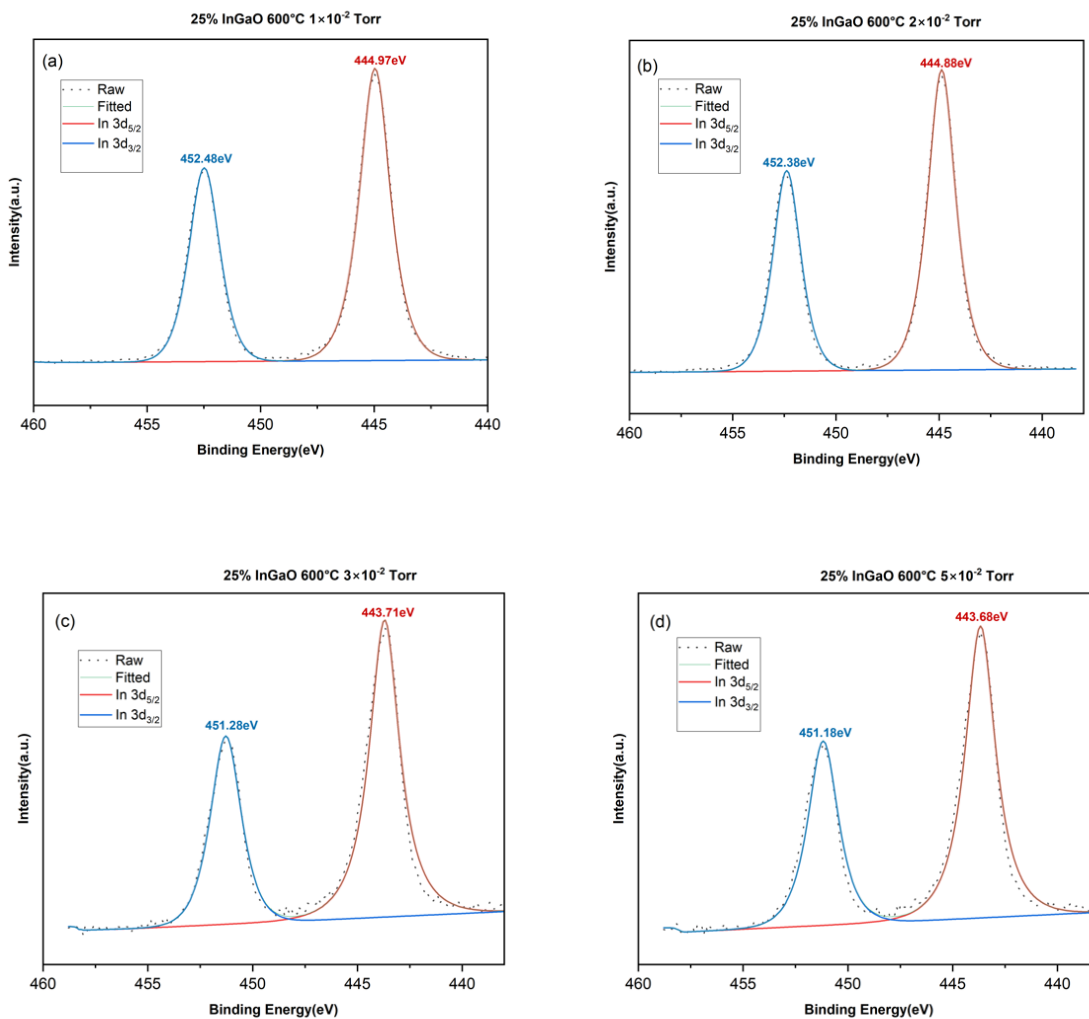


Figure 4.10: High resolution In 3d core level XPS spectra of $(\text{InGa})_2\text{O}_3$ for various oxygen partial pressure (a) 1×10^{-2} torr (b) 2×10^{-2} torr (c) 3×10^{-2} torr and (d) 5×10^{-2} torr respectively with a fixed substrate temperature of 600°C .

Figure 4.11 shows the high-resolution XPS scan of the Ga 3d peaks for various oxygen partial pressure with a fixed substrate temperature of 600°C . The peak located around 20 eV is assigned to the fully oxidized Ga^{3+} state. There is no significant shift in Ga core levels with the increase of partial oxygen pressure. Thus, Ga 3d peak scan has no effect on the change in mobility with pressure.

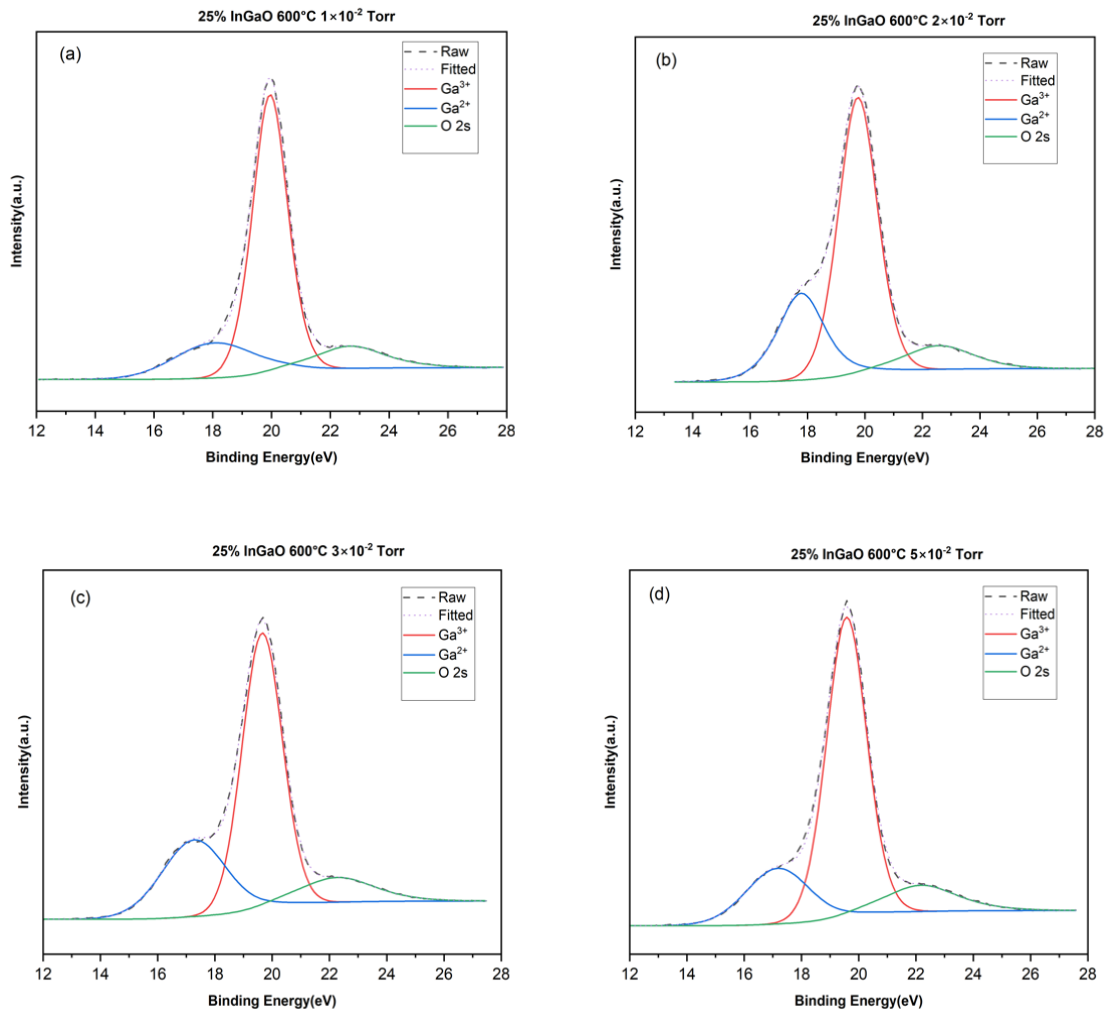


Figure 4.11: High resolution Ga3d_{5/2} XPS spectra of (InGa)₂O₃ for various oxygen partial pressure (a) 1×10⁻² torr (b) 2×10⁻² torr (c) 3×10⁻² torr and (d) 5×10⁻² torr respectively with a fixed substrate temperature of 600°C.

4.3 Effect of homoepitaxial buffer layer on defect reduction in $(\text{In}_x\text{Ga}_{1-x})_2\text{O}_3$ alloy

To investigate the effect of the implementation of buffer layer on mobility and defect, $(\text{In}_x\text{Ga}_{1-x})_2\text{O}_3$ alloys ($x=25\%$) were deposited on sapphire substrate with a Ga_2O_3 buffer layer. In order to compare these films with the films grown without the buffer layer, the growth condition was selected as 600°C substrate temperature, 5×10^{-2} torr oxygen partial pressure, and 500°C substrate temperature and 3×10^{-2} torr oxygen partial pressure respectively. As the highest mobility and the lowest resistivity were achieved at these growth conditions for crystalline and amorphous samples, similar growth condition was fixed for the deposition of the films with Ga_2O_3 buffer layer. Figure 4.12 shows the high-resolution XRD 2θ - ω scans of $(\text{InGa})_2\text{O}_3$ (IGO) thin films with and without buffer layer.

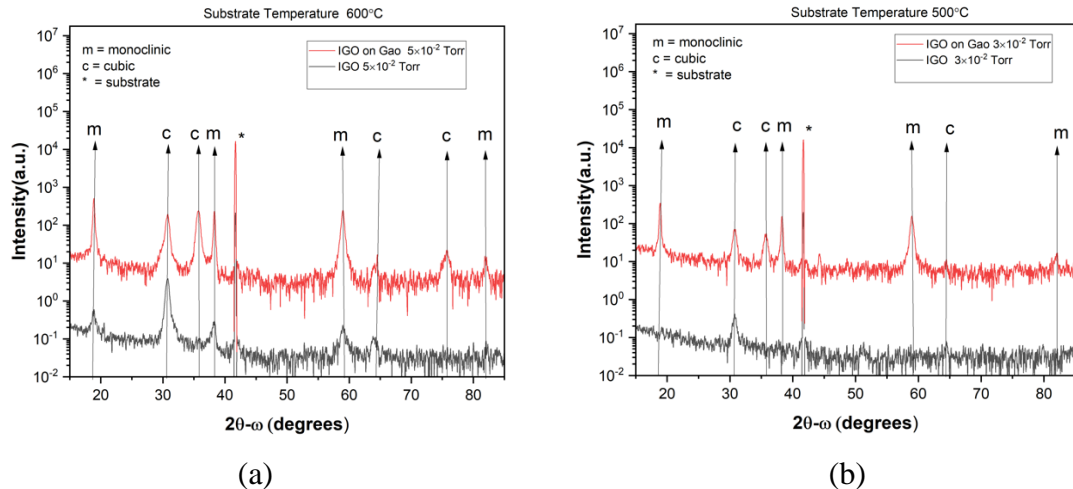


Figure 4.12: XRD measurement of $(\text{InGa})_2\text{O}_3$ thin films with and without buffer layer grown at (a) substrate temperature of 600°C and oxygen partial pressure of 5×10^{-2} torr (b) substrate temperature of 500°C and oxygen partial pressure of 3×10^{-2} torr.

The XRD analysis of figure 4.12(a) shows higher intensity for both the monoclinic and cubic peaks with some additional cubic phases for the films grown with the buffer layer. Figure 4.12(b) shows that the film transitions from almost amorphous to

crystalline phase when deposited with the buffer layer as both monoclinic and cubic peaks are detected here. After that temperature dependent Hall analysis was performed to compare the mobility and resistivity for both conditions. Figure 4.13 and figure 4.14 depict temperature vs resistivity and temperature vs mobility respectively from where the comparative analysis of the films with and without buffer layer can be described. For the crystalline films grown at 600°C substrate temperature, the resistivity decreases when the film grown with homoepitaxial buffer layer which is shown in figure 4.13(a) and films grown with buffer layer shows an increase in mobility and it is shown in figure 4.14(a). But for the films grown at 500°C substrate temperature, the opposite result is observed. As depositing with buffer layer, the amorphous films increased in crystallinity. This could be explained by the film having an increase in grain boundaries and crystalline defects when compared to an amorphous film.

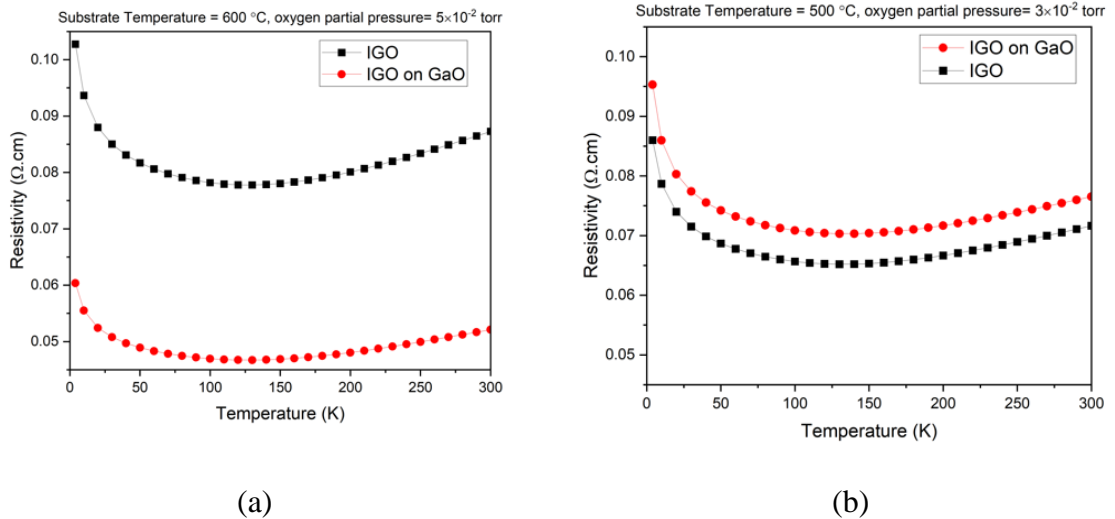


Figure 4.13: Temperature vs resistivity measurement of (InGa)₂O₃ thin films with and without buffer layer grown at (a) substrate temperature=600°C and oxygen partial pressure=5×10⁻² torr (b) substrate temperature=500°C and oxygen partial pressure=3×10⁻² torr.

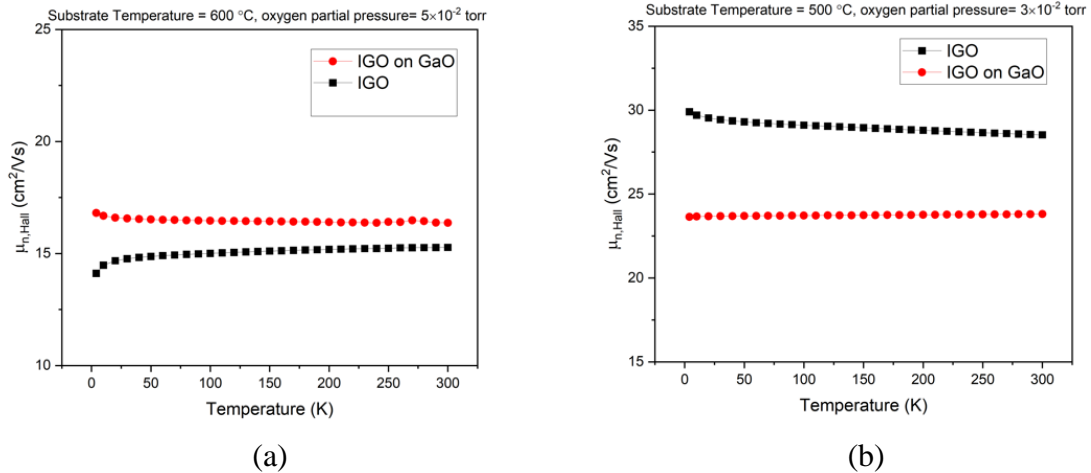


Figure 4.14: Temperature vs mobility measurement of $(\text{InGa})_2\text{O}_3$ thin films with and without buffer layer grown at (a) substrate temperature= 600°C and oxygen partial pressure= 5×10^{-2} torr (b) substrate temperature= 500°C and oxygen partial pressure= 3×10^{-2} torr.

Finally, the XPS analysis revealed that for film grown at 600°C with a buffer layer has its O_{II} peak shifted to the lower binding energy state compared to the film grown without the buffer layer. As the shift of peak to the lower binding energy is attributed to the reduction of internal defects via oxygen vacancy reduction, it can be said from figure 4.15 that defect is mitigated by implementing the homoepitaxial buffer layer for crystalline films. Thus, the mobility was increased as shown in figure 4.14(a). On the other hand, because of the phase change of previously observed amorphous films, the effect of the homoepitaxial buffer layer on the change of binding energy cannot be compared with the previously analyzed data. Figure 4.16 shows that the film without buffer layer has lower binding energy peak shift compared to the other one.

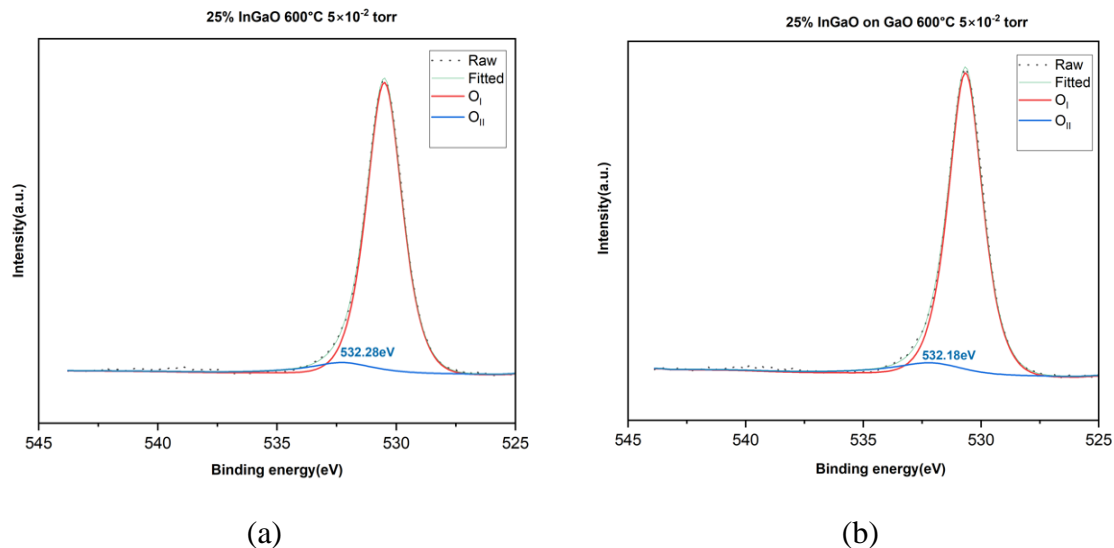


Figure 4.15: High resolution O1s core level XPS spectra of (InGa)₂O₃ grown at fixed substrate temperature of 600°C and oxygen partial pressure of 5×10⁻² torr (a) without buffer layer (b) with buffer layer.

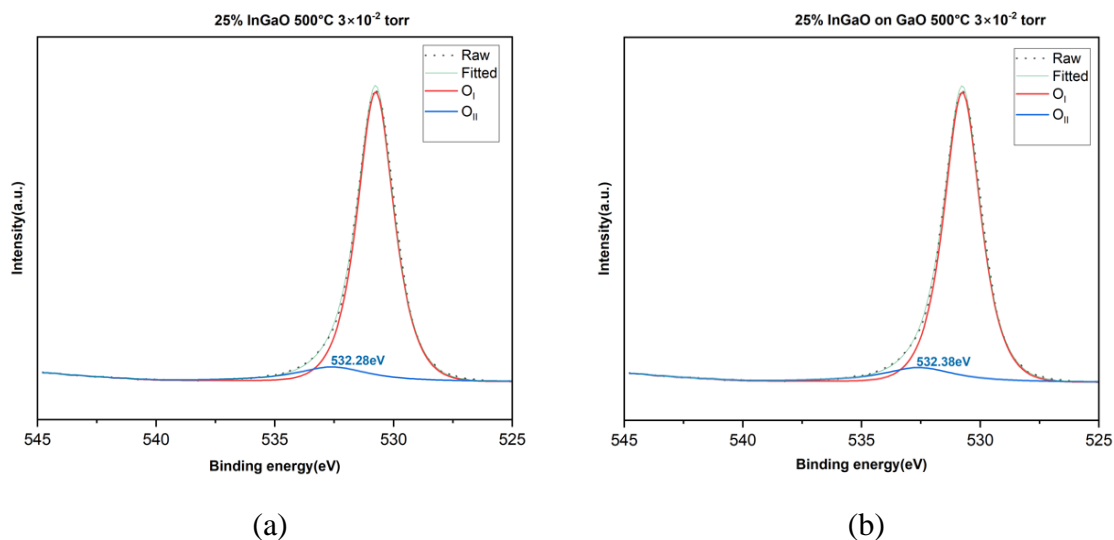


Figure 4.16: High resolution O1s core level XPS spectra of (InGa)₂O₃ grown at fixed substrate temperature of 500°C and oxygen partial pressure of 3×10⁻² torr (a) without buffer layer (b) with buffer layer.

5. CONCLUSION AND FUTURE WORK

Indium gallium oxide alloy is one of the most promising candidates for the next generation of power devices because of its bandgap tunable properties in the wide bandgap region. Structural and compositional understanding of alloys like indium gallium oxide is thus important. This research demonstrates the deposition of ternary $(\text{In}_x\text{Ga}_{1-x})_2\text{O}_3$ alloys with $x=25\%$ on c-plane sapphire using pulsed laser deposition by varying growth conditions such as substrate temperature and oxygen partial pressure. The structural property of the as-grown layers was studied based on the growth parameters employing x-ray diffraction (XRD) analysis. At substrate temperatures above 500°C , both monoclinic and cubic bixbyite phases were detected which indicated the crystalline phase of the $(\text{In}_x\text{Ga}_{1-x})_2\text{O}_3$ thin films. But $\leq 500^\circ\text{C}$ of substrate temperature, no significant peak was found representing an amorphous phase of the films when grown at lower substrate temperatures. The thickness was measured by spectroscopic ellipsometry and a slight variation in the thickness was observed possibly because of the evaporation of volatile Ga_2O and In_2O suboxides at elevated temperatures. The resistivity and mobility for both the amorphous and crystalline films were determined using temperature dependent Hall measurement analysis. The mobility was found to be increasing with increasing thickness. The mobility and resistivity of the alloys are of the order $\sim 14\text{-}30\text{ cm}^2/\text{Vs}$ and $\sim 7\times 10^{-2}\text{-}9\times 10^{-2}\ \Omega\cdot\text{cm}$ respectively. For the crystalline films, the mobility was increased with the increase of oxygen partial pressure. Amorphous samples were found to have higher mobilities compared to the crystalline films due to having higher thickness value and reduction of grain boundary scattering. Finally, to investigate the reason of change in mobility with increasing oxygen pressure, XPS analysis was performed. A

mixture of Ga and In cations valence state denoted the oxidation states of Ga and In. The shift of the oxygen peak to the lower binding energy with increased oxygen pressure indicated the reduction of the oxygen vacancies which in turn results in the mitigation of internal defects due to the oxygen vacancies. Thus, oxygen vacancy reduction can also be a viable reason behind the increase of mobility with oxygen partial pressure for the crystalline films. The reduction of the oxygen peak intensity was also attributed to the reduction of oxygen vacancies. As the amorphous samples had lower oxygen peak intensity compared to the crystalline samples, the mobility of the amorphous films was higher than that of the crystalline films. To investigate more on the possible effects on the reduction of internal defects, $(\text{In}_x\text{Ga}_{1-x})_2\text{O}_3$ ($x=25\%$) alloys were grown on sapphire substrate with a Ga_2O_3 buffer layer and all the similar characteristic analysis were performed to provide a comparative analysis. By reducing the internal defects, using the homoepitaxial buffer layer an increase in mobility for the crystalline alloys was observed. Further investigation to the root cause of change in mobility in $(\text{In}_x\text{Ga}_{1-x})_2\text{O}_3$ thin films grown in different PLD chamber environment can lead to the state-of-the-art electronic device innovation in power electronics area.

Future work includes the investigation into the cause of defects originated in $(\text{In}_x\text{Ga}_{1-x})_2\text{O}_3$ thin films by C-V measurement. The effect of the variation of indium composition in the $(\text{In}_x\text{Ga}_{1-x})_2\text{O}_3$ thin films on the change of mobility is worthy of further studies. Finally electronic devices fabricated with superlattice structures of $(\text{In}_x\text{Ga}_{1-x})_2\text{O}_3$ should be investigated to demonstrate the potential of this bandgap tunable alloy.

REFERENCES

- [1] T. C. Lovejoy, "III-VI semiconductors and oxides: Electronic structure, surface morphology, and transition metal doping of gallium selenide, indium selenide, and gallium oxide - ProQuest," University of Washington, 2010.
- [2] L. Shi and S. Nihtianov, "Comparative Study of Silicon-Based Ultraviolet Photodetectors," *IEEE Sens. J.*, vol. 12, no. 7, pp. 2453–2459, Jul. 2012, doi: 10.1109/JSEN.2012.2192103.
- [3] T.-C. Wei *et al.*, "See-Through Ga_2O_3 Solar-Blind Photodetectors for Use in Harsh Environments," *IEEE J. Sel. Top. Quantum Electron.*, vol. 20, no. 6, pp. 112–117, Nov. 2014, doi: 10.1109/JSTQE.2014.2321517.
- [4] E. Monroy, F. Omnès, and F. Calle, "Wide-bandgap semiconductor ultraviolet photodetectors," *Semicond. Sci. Technol.*, vol. 18, no. 4, p. R33, Mar. 2003, doi: 10.1088/0268-1242/18/4/201.
- [5] J. B. Varley, J. R. Weber, A. Janotti, and C. G. Van de Walle, "Oxygen vacancies and donor impurities in $\beta\text{-Ga}_2\text{O}_3$," *Appl. Phys. Lett.*, vol. 97, no. 14, p. 142106, Oct. 2010, doi: 10.1063/1.3499306.
- [6] K. Kajiyama and H. Kanbe, "Temperature dependence of avalanche breakdown voltage in Si p-n junctions," *J. Appl. Phys.*, vol. 47, no. 6, pp. 2744–2745, Jun. 1976, doi: 10.1063/1.322999.
- [7] J. L. Hudgins, G. S. Simin, E. Santi, and M. A. Khan, "An assessment of wide bandgap semiconductors for power devices," *IEEE Trans. Power Electron.*, vol. 18, no. 3, pp. 907–914, May 2003, doi: 10.1109/TPEL.2003.810840.
- [8] G. Giusti, "Deposition and characterisation of functional ITO thin films," *d_ph*, University of Birmingham, 2011. Accessed: Nov. 02, 2022. [Online]. Available: <https://etheses.bham.ac.uk/id/eprint/1678/>.
- [9] S. I. Stepanov, V. I. Nikolaev, V. E. Bougrov, and A. E. Romanov, "GALLIUM OXIDE: PROPERTIES AND APPLICA 498 A REVIEW," *Rev Adv Mater Sci*, vol. 44, pp. 63–86.
- [10] M. Higashiwaki and G. H. Jessen, "Guest Editorial: The dawn of gallium oxide microelectronics," *Appl. Phys. Lett.*, vol. 112, no. 6, p. 060401, Feb. 2018, doi: 10.1063/1.5017845.
- [11] H. Akazawa, "Formation of various phases of gallium oxide films depending on substrate planes and deposition gases," *Vacuum*, vol. 123, pp. 8–16, Jan. 2016, doi: 10.1016/j.vacuum.2015.10.009.

- [12] H. F. Mohamed, C. Xia, Q. Sai, H. Cui, M. Pan, and H. Qi, "Growth and fundamentals of bulk β -Ga₂O₃ single crystals," *J. Semicond.*, vol. 40, no. 1, p. 011801, Jan. 2019, doi: 10.1088/1674-4926/40/1/011801.
- [13] M. Higashiwaki, K. Sasaki, A. Kuramata, T. Masui, and S. Yamakoshi, "Gallium oxide (Ga₂O₃) metal-semiconductor field-effect transistors on single-crystal β -Ga₂O₃ (010) substrates," *Appl. Phys. Lett.*, vol. 100, no. 1, p. 013504, Jan. 2012, doi: 10.1063/1.3674287.
- [14] E. G. Villora, K. Shimamura, Y. Yoshikawa, T. Ujiie, and K. Aoki, "Electrical conductivity and carrier concentration control in β -Ga₂O₃ by Si doping," *Appl. Phys. Lett.*, vol. 92, no. 20, p. 202120, May 2008, doi: 10.1063/1.2919728.
- [15] M. J. Tadjer, J. L. Lyons, N. Nepal, J. A. Freitas, A. D. Koehler, and G. M. Foster, "Editors' Choice—Review—Theory and Characterization of Doping and Defects in β -Ga₂O₃," *ECS J. Solid State Sci. Technol.*, vol. 8, no. 7, p. Q3187, Mar. 2019, doi: 10.1149/2.0341907jss.
- [16] F. Zhang, K. Saito, T. Tanaka, M. Nishio, M. Arita, and Q. Guo, "Wide bandgap engineering of (AlGa)₂O₃ films," *Appl. Phys. Lett.*, vol. 105, no. 16, p. 162107, Oct. 2014, doi: 10.1063/1.4900522.
- [17] M. D. Mia, "Growth and Characterization of Ga₂O₃ (Ga_{1-x}Gdx)₂O₃ and (Ga_{1-x}Fex)₂O₃ Thin Films by Pulsed Laser Deposition," Aug. 2020, Accessed: Nov. 02, 2022. [Online]. Available: <https://digital.library.txstate.edu/handle/10877/15185>.
- [18] S. Ghose, "Growth and Characterization of Wide Bandgap Semiconductor Oxide Thin Films," 2017. Accessed: Nov. 02, 2022. [Online]. Available: <https://ui.adsabs.harvard.edu/abs/2017PhDT.....109G>.
- [19] Y. Yao *et al.*, "Growth and characterization of α -, β -, and ϵ -phases of Ga₂O₃ using MOCVD and HVPE techniques," *Mater. Res. Lett.*, vol. 6, no. 5, pp. 268–275, May 2018, doi: 10.1080/21663831.2018.1443978.
- [20] J. Åhman, G. Svensson, and J. Albertsson, "A Reinvestigation of β -Gallium Oxide," *Acta Crystallogr. C*, vol. 52, no. 6, Art. no. 6, Jun. 1996, doi: 10.1107/S0108270195016404.
- [21] S. Geller, "Crystal Structure of β -Ga₂O₃," *J. Chem. Phys.*, vol. 33, no. 3, pp. 676–684, Sep. 1960, doi: 10.1063/1.1731237.
- [22] H. Peelaers and C. G. Van de Walle, "Brillouin zone and band structure of β -Ga₂O₃," *Phys. Status Solidi B*, vol. 252, no. 4, pp. 828–832, 2015, doi: 10.1002/pssb.201451551.

- [23] F. Shi and H. Qiao, “Preparations, properties and applications of gallium oxide nanomaterials – A review,” *Nano Sel.*, vol. 3, no. 2, pp. 348–373, 2022, doi: 10.1002/nano.202100149.
- [24] M. Higashiwaki, K. Sasaki, A. Kuramata, T. Masui, and S. Yamakoshi, “Development of gallium oxide power devices,” *Phys. Status Solidi A*, vol. 211, no. 1, pp. 21–26, 2014, doi: 10.1002/pssa.201330197.
- [25] N. Ueda, H. Hosono, R. Waseda, and H. Kawazoe, “Synthesis and control of conductivity of ultraviolet transmitting β -Ga₂O₃ single crystals,” *Appl. Phys. Lett.*, vol. 70, no. 26, pp. 3561–3563, Jun. 1997, doi: 10.1063/1.119233.
- [26] Z. Galazka, “Growth of bulk β -Ga₂O₃ single crystals by the Czochralski method,” *J. Appl. Phys.*, vol. 131, no. 3, p. 031103, Jan. 2022, doi: 10.1063/5.0076962.
- [27] Z. Guo *et al.*, “Anisotropic thermal conductivity in single crystal β -gallium oxide,” *Appl. Phys. Lett.*, vol. 106, no. 11, p. 111909, Mar. 2015, doi: 10.1063/1.4916078.
- [28] E. G. Villora, K. Shimamura, T. Ujiie, and K. Aoki, “Electrical conductivity and lattice expansion of β -Ga₂O₃ below room temperature,” *Appl. Phys. Lett.*, vol. 92, no. 20, p. 202118, May 2008, doi: 10.1063/1.2910770.
- [29] M. Higashiwaki *et al.*, “Recent progress in Ga₂O₃ power devices,” *Semicond. Sci. Technol.*, vol. 31, no. 3, p. 034001, Jan. 2016, doi: 10.1088/0268-1242/31/3/034001.
- [30] K. Irmscher, Z. Galazka, M. Pietsch, R. Uecker, and R. Fornari, “Electrical properties of β -Ga₂O₃ single crystals grown by the Czochralski method,” *J. Appl. Phys.*, vol. 110, no. 6, p. 063720, Sep. 2011, doi: 10.1063/1.3642962.
- [31] N. Ma *et al.*, “Intrinsic electron mobility limits in β -Ga₂O₃,” *Appl. Phys. Lett.*, vol. 109, no. 21, p. 212101, Nov. 2016, doi: 10.1063/1.4968550.
- [32] T. Onuma *et al.*, “Polarized Raman spectra in β -Ga₂O₃ single crystals,” *J. Cryst. Growth*, vol. 401, pp. 330–333, Sep. 2014, doi: 10.1016/j.jcrysgro.2013.12.061.
- [33] H. He, M. A. Blanco, and R. Pandey, “Electronic and thermodynamic properties of β -Ga₂O₃,” *Appl. Phys. Lett.*, vol. 88, no. 26, p. 261904, Jun. 2006, doi: 10.1063/1.2218046.
- [34] L. L. Liu *et al.*, “Fabrication and characteristics of N-doped β -Ga₂O₃ nanowires,” *Appl. Phys. A*, vol. 98, no. 4, pp. 831–835, Mar. 2010, doi: 10.1007/s00339-009-5538-y.

- [35] L. Zhang, J. Yan, Y. Zhang, T. Li, and X. Ding, “First-principles study on electronic structure and optical properties of N-doped P-type β -Ga₂O₃,” *Sci. China Phys. Mech. Astron.*, vol. 55, no. 1, pp. 19–24, Jan. 2012, doi: 10.1007/s11433-011-4582-8.
- [36] H. Kawazoe, H. Yanagi, K. Ueda, and H. Hosono, “Transparent p-Type Conducting Oxides: Design and Fabrication of p-n Heterojunctions,” *MRS Bull.*, vol. 25, no. 8, pp. 28–36, Aug. 2000, doi: 10.1557/mrs2000.148.
- [37] J. B. Varley, A. Janotti, C. Franchini, and C. G. Van de Walle, “Role of self-trapping in luminescence and p -type conductivity of wide-band-gap oxides,” *Phys. Rev. B*, vol. 85, no. 8, p. 081109, Feb. 2012, doi: 10.1103/PhysRevB.85.081109.
- [38] S. Shanmugan, D. Mutharasu, and I. Kamarulazizi, “Rhombohedral In₂O₃ thin films preparation from in metal film using Oxygen plasma,” in *2012 10th IEEE International Conference on Semiconductor Electronics (ICSE)*, Sep. 2012, pp. 711–715. doi: 10.1109/SMElec.2012.6417242.
- [39] M. F. Bekheet *et al.*, “Orthorhombic In₂O₃: A Metastable Polymorph of Indium Sesquioxide,” *Angew. Chem. Int. Ed.*, vol. 52, no. 25, pp. 6531–6535, 2013, doi: 10.1002/anie.201300644.
- [40] T. de Boer, M. F. Bekheet, A. Gurlo, R. Riedel, and A. Moewes, “Band gap and electronic structure of cubic, rhombohedral, and orthorhombic In_2O_3 polymorphs: Experiment and theory,” *Phys. Rev. B*, vol. 93, no. 15, p. 155205, Apr. 2016, doi: 10.1103/PhysRevB.93.155205.
- [41] S. Zh. Karazhanov, P. Ravindran, P. Vajeeston, A. Ulyashin, T. G. Finstad, and H. Fjellvåg, “Phase stability, electronic structure, and optical properties of indium oxide polytypes,” *Phys. Rev. B*, vol. 76, no. 7, p. 075129, Aug. 2007, doi: 10.1103/PhysRevB.76.075129.
- [42] R. L. Weiher and R. P. Ley, “Optical Properties of Indium Oxide,” *J. Appl. Phys.*, vol. 37, no. 1, pp. 299–302, Jan. 1966, doi: 10.1063/1.1707830.
- [43] P. D. C. King, T. D. Veal, D. J. Payne, A. Bourlange, R. G. Egdell, and C. F. McConville, “Surface Electron Accumulation and the Charge Neutrality Level in In_2O_3 ,” *Phys. Rev. Lett.*, vol. 101, no. 11, p. 116808, Sep. 2008, doi: 10.1103/PhysRevLett.101.116808.
- [44] J. H. W. de Wit, “The high temperature behavior of In₂O₃,” *J. Solid State Chem.*, vol. 13, no. 3, pp. 192–200, Mar. 1975, doi: 10.1016/0022-4596(75)90118-8.

- [45] P. Ágoston, P. Erhart, A. Klein, and K. Albe, “Geometry, electronic structure and thermodynamic stability of intrinsic point defects in indium oxide,” *J. Phys. Condens. Matter*, vol. 21, no. 45, p. 455801, Oct. 2009, doi: 10.1088/0953-8984/21/45/455801.
- [46] O. Bierwagen, “Indium oxide—a transparent, wide-band gap semiconductor for (opto)electronic applications,” *Semicond. Sci. Technol.*, vol. 30, no. 2, p. 024001, Jan. 2015, doi: 10.1088/0268-1242/30/2/024001.
- [47] T. Minami, Y. Takeda, T. Kakumu, S. Takata, and I. Fukuda, “Preparation of highly transparent and conducting Ga₂O₃–In₂O₃ films by direct current magnetron sputtering,” *J. Vac. Sci. Technol. A*, vol. 15, no. 3, pp. 958–962, May 1997, doi: 10.1116/1.580787.
- [48] J. M. Phillips *et al.*, “Transparent conducting thin films of GaInO₃,” *Appl. Phys. Lett.*, vol. 65, no. 1, pp. 115–117, Jul. 1994, doi: 10.1063/1.113052.
- [49] F. Zhang, K. Saito, T. Tanaka, M. Nishio, and Q. Guo, “Wide bandgap engineering of (GaIn)₂O₃ films,” *Solid State Commun.*, vol. 186, pp. 28–31, May 2014, doi: 10.1016/j.ssc.2014.01.024.
- [50] T. Oshima and S. Fujita, “Properties of Ga₂O₃-based (In_x Ga_{1-x})₂O₃ alloy thin films grown by molecular beam epitaxy,” *Phys. Status Solidi C*, vol. 5, no. 9, pp. 3113–3115, 2008, doi: 10.1002/pssc.200779297.
- [51] H. von Wenckstern *et al.*, “Structural and optical properties of (In,Ga)₂O₃ thin films and characteristics of Schottky contacts thereon,” *Semicond. Sci. Technol.*, vol. 30, no. 2, p. 024005, Jan. 2015, doi: 10.1088/0268-1242/30/2/024005.
- [52] F. Zhang *et al.*, “Toward the understanding of annealing effects on (GaIn)₂O₃ films,” *Thin Solid Films*, vol. 578, pp. 1–6, Mar. 2015, doi: 10.1016/j.tsf.2015.02.003.
- [53] S.-P. Chang, L.-Y. Chang, and J.-Y. Li, “The Influence of Different Partial Pressure on the Fabrication of InGaO Ultraviolet Photodetectors,” *Sensors*, vol. 16, no. 12, Art. no. 12, Dec. 2016, doi: 10.3390/s16122145.
- [54] J. A. Greer, “History and current status of commercial pulsed laser deposition equipment,” *J. Phys. Appl. Phys.*, vol. 47, no. 3, p. 034005, Dec. 2013, doi: 10.1088/0022-3727/47/3/034005.
- [55] A. Khan, F. Rahman, R. Nongjai, and K. Asokan, “Optical transmittance and electrical transport investigations of Fe-doped In₂O₃ thin films,” *Appl. Phys. A*, vol. 127, no. 5, p. 339, Apr. 2021, doi: 10.1007/s00339-021-04490-0.

- [56] M. N. R. Ashfold, F. Claeysens, G. M. Fuge, and S. J. Henley, “Pulsed laser ablation and deposition of thin films,” *Chem. Soc. Rev.*, vol. 33, no. 1, pp. 23–31, Dec. 2004, doi: 10.1039/B207644F.
- [57] M. G. Norton and C. B. Carter, “On the optimization of the laser ablation process for the deposition of YBa₂Cu₃O_{7-δ} thin films,” *Phys. C Supercond.*, vol. 172, no. 1, pp. 47–56, Dec. 1990, doi: 10.1016/0921-4534(90)90641-Q.
- [58] M. Lee, *X-Ray Diffraction for Materials Research: From Fundamentals to Applications*. New York: Apple Academic Press, 2017. doi: 10.1201/b19936.
- [59] T. Sochi, “High Throughput Software for Powder Diffraction and its Application to Heterogeneous Catalysis.” arXiv, Dec. 20, 2010. doi: 10.48550/arXiv.1012.4506.
- [60] H. Fujiwara, *Spectroscopic Ellipsometry: Principles and Applications*. John Wiley & Sons, 2007.
- [61] B. Juergen and P. Alexey, “Fast polarization state detection by division-of-amplitude in a simple configuration setup,” in *Proceedings of the 2015 Joint Workshop of Fraunhofer IOSB and Institute for Anthropomatics*, Jul. 2016, vol. 24.
- [62] M. Schubert, “Another century of ellipsometry *,” *Ann. Phys.*, vol. 518, no. 7–8, pp. 480–497, 2006, doi: 10.1002/andp.200651807-805.
- [63] T. Minamikawa *et al.*, “Dual-comb spectroscopic ellipsometry,” *Nat. Commun.*, vol. 8, no. 1, Art. no. 1, Sep. 2017, doi: 10.1038/s41467-017-00709-y.
- [64] “Resistivity and Hall Measurements,” *NIST*, Apr. 2010, Accessed: Nov. 02, 2022. [Online]. Available: <https://www.nist.gov/pml/nanoscale-device-characterization-division/popular-links/hall-effect/resistivity-and-hall>
- [65] “Electron Spectroscopy,” in *An Introduction to Surface Analysis by XPS and AES*, John Wiley & Sons, Ltd, 2019, pp. 1–18. doi: 10.1002/9781119417651.ch1.
- [66] F. A. Stevie and C. L. Donley, “Introduction to x-ray photoelectron spectroscopy,” *J. Vac. Sci. Technol. A*, vol. 38, no. 6, p. 063204, Dec. 2020, doi: 10.1116/6.0000412.
- [67] Y. H. Hwang and B.-S. Bae, “Effect of Aluminum and Gallium Doping on the Performance of Solution-Processed Indium Oxide Thin-Film Transistors,” *J. Disp. Technol.*, vol. 9, no. 9, pp. 704–709, Sep. 2013, doi: 10.1109/JDT.2013.2255260.

- [68] H. J. Park, T. Kim, M. J. Kim, H. Lee, J. H. Lim, and J. K. Jeong, "Improvement in performance of indium gallium oxide thin film transistor via oxygen mediated crystallization at a low temperature of 200 °C," *Ceram. Int.*, vol. 48, no. 9, pp. 12806–12812, May 2022, doi: 10.1016/j.ceramint.2022.01.151.
- [69] S. Kaleemulla, A. S. Reddy, S. Uthanna, and P. S. Reddy, "Physical properties of In₂O₃ thin films prepared at various oxygen partial pressures," *J. Alloys Compd.*, vol. 479, no. 1, pp. 589–593, Jun. 2009, doi: 10.1016/j.jallcom.2009.01.003.
- [70] H. Nishinaka, H. Komai, D. Tahara, Y. Arata, and M. Yoshimoto, "Microstructures and rotational domains in orthorhombic ϵ -Ga₂O₃ thin films," *Jpn. J. Appl. Phys.*, vol. 57, no. 11, p. 115601, Oct. 2018, doi: 10.7567/JJAP.57.115601.
- [71] V. Gottschalch *et al.*, "Heteroepitaxial growth of α -, β -, γ - and κ -Ga₂O₃ phases by metalorganic vapor phase epitaxy," *J. Cryst. Growth*, vol. 510, pp. 76–84, Mar. 2019, doi: 10.1016/j.jcrysgro.2019.01.018.
- [72] M. Kneiß *et al.*, "Epitaxial stabilization of single phase κ -(In_xGa_{1-x})₂O₃ thin films up to x = 0.28 on c-sapphire and κ -Ga₂O₃(001) templates by tin-assisted VCCS-PLD," *APL Mater.*, vol. 7, no. 10, p. 101102, Oct. 2019, doi: 10.1063/1.5120578.
- [73] A. Hassa *et al.*, "Structural, optical, and electrical properties of orthorhombic κ -(In_xGa_{1-x})₂O₃ thin films," *APL Mater.*, vol. 7, no. 2, p. 022525, Feb. 2019, doi: 10.1063/1.5054394.
- [74] X. Wang *et al.*, "Influence of substrate temperature on the properties of (AlGa)₂O₃ thin films prepared by pulsed laser deposition," *Ceram. Int.*, vol. 42, no. 11, pp. 12783–12788, Aug. 2016, doi: 10.1016/j.ceramint.2016.05.039.
- [75] F. B. Zhang, K. Saito, T. Tanaka, M. Nishio, and Q. X. Guo, "Structural and optical properties of Ga₂O₃ films on sapphire substrates by pulsed laser deposition," *J. Cryst. Growth*, vol. 387, pp. 96–100, Feb. 2014, doi: 10.1016/j.jcrysgro.2013.11.022.
- [76] S.-H. Yuan, S.-L. Ou, C.-M. Chen, S.-Y. Huang, B.-W. Hsiao, and D.-S. Wu, "Characterization of aluminum gallium oxide films grown by pulsed laser deposition," *Ceram. Int.*, vol. 45, no. 1, pp. 702–707, Jan. 2019, doi: 10.1016/j.ceramint.2018.09.232.
- [77] J. Chen, L. Wang, X. Su, L. Kong, G. Liu, and X. Zhang, "InGaZnO semiconductor thin film fabricated using pulsed laser deposition," *Opt. Express*, vol. 18, no. 2, pp. 1398–1405, Jan. 2010, doi: 10.1364/OE.18.001398.
- [78] Y.-C. Cheng *et al.*, "Stability Improvement of Nitrogen Doping on IGO TFTs under Positive Gate Bias Stress and Hysteresis Test," *ECS J. Solid State Sci. Technol.*, vol. 8, no. 7, p. Q3034, Feb. 2019, doi: 10.1149/2.0081907jss.

- [79] H. Pu, Q. Zhou, L. Yue, and Q. Zhang, "Investigation of oxygen plasma treatment on the device performance of solution-processed a-IGZO thin film transistors," *Appl. Surf. Sci.*, vol. 283, pp. 722–726, Oct. 2013, doi: 10.1016/j.apsusc.2013.07.007.
- [80] G. G. Khan *et al.*, "Defect engineered d0 ferromagnetism in tin-doped indium oxide nanostructures and nanocrystalline thin-films," *J. Appl. Phys.*, vol. 118, no. 7, p. 074303, Aug. 2015, doi: 10.1063/1.4928952.